



UNIVERSITEIT VAN PRETORIA
UNIVERSITY OF PRETORIA
YUNIBESITHI YA PRETORIA

Characterization of SANS Facility at Necsa and SANS Application to the Study of Wool Fibres

by

Tjatji Calvin Tjebane

Submitted in partial fulfilment of the requirements for a degree of

MAGISTER SCIENTIAE

in the Faculty of Natural and Agricultural Sciences at University
of Pretoria

Supervisor: Prof. C.C. Theron

Co-Supervisor: Dr. C.B. Franklyn

February 2015

Declaration

I, Tjatji Calvin Tjebane, with student number u12000257, declare that:

- I understand what plagiarism is and am aware of the University's policy in this regard.
- To the best of my knowledge and belief this thesis contains no material previously published by any other person except where due acknowledgement has been made.
- The dissertation has not been previously submitted by me or anyone for any other degree or diploma at this or any other tertiary institution.

Signature:.....

Acknowledgements

I wish to thank the following people and organisations who directly contributed to the success of this project. Their knowledgeable advice, suggestions and comments made the research and the write-up all the more enjoyable:

Prof. C. Theron from UP, with his endless advice and patience.

Dr. C. Franklyn, ever-present next door, who always gave me a guilt-conscience when I felt tired and thought of quitting.

Dr. G. Török for making sure beam time at Budapest Neutron Scattering (BNC) is allocated and experiments were prepared and ran successfully. He also made a valuable input in analysing the SANS data and modelling of the facility.

Being an experimentalist, you also need technical support in terms of electronics, mechanical and computing thus not mentioning the following, will just look as if the project was executed in the backyard, which is highly impossible:

- Mr. D. Buys and P. Pare for their electronics support,
- Mr. V. Rababalela, Mr. E. Homann, Mr. G. Young and Mr. L. Malematsha for their mechanical support,

- Safari-1 team, who were always available for the execution of the tasks outside of their prescribed work, without complains, and
- Mr. J-P. Taylor for always being there to tirelessly help me fix bugs on the word processor I used to present this work.

This project would not have been possible without the financial support from the following institutions:

- International Atomic Energy Agency (IAEA) for their equipment support in making the SANS facility a success as well as their financial support to attend training in neutron scattering techniques and applications.
- South African Nuclear Energy Corporation (Necsa) and National Research Foundation (NRF) mobility grant for trip to Budapest working visit as well as support towards my studies.

This dissertation is dedicated to my late mother – Ramaabele Moela, who always believed in me. ”Rest in peace mom, I will always strive to shine as you proved everything is possible.” Also to my father Maphadime Tjebane who always made me not to loose hope. ”Thanks for being there all the times dad, when our relationship turned into a friendship where we could talk about anything and everything without me being hesitant –*Morwaswi 'a Ngwato, o gole o kake tlou, gomme tšhukudu ebe mošimane.* I’m blessed for still having you around”

Finally, thanks to my wife - Yvonne, and my three beautiful daughters - Chantelle, Lesego and Lethabo for their unfailing support and interest in my

work, and their understanding of me spending time away without them to compile this work.

Abstract

A short-version (~ 10 m) Small Angle Neutron Scattering (SANS) beam line facility was installed at the South African Nuclear Energy Corporation (Necsa)'s SAFARI-1 Research Reactor. This was in a way to prepare for a practical low signal-to-noise ratio SANS at Necsa, although there is no cold source nor available tangential beam channel, the beam line has been installed on a radial beam channel. A low signal-to-noise ratio SANS is possible by using curved neutron guides and a long scattering chamber to observe a broad momentum transfer range with minimal use of radiation shielding. In this work, Silver Behenate ($\text{AgC}_{22}\text{H}_{43}\text{O}_2$) was used as a standard sample for calibrating the small-angle scattering instruments to calibrate the short-version SANS facility. The results were compared with those from a similar facility at the Budapest Neutron Centre (BNC) in Hungary.

Using the BNC SANS facility, a study of wool and mohair fibre properties during the wetting process was also performed. The process has been exploited by different techniques, especially Small Angle X-ray Scattering (SAXS). Although the macroscopic wetting process is well understood, observation of the exact location of the water accumulation has not been confirmed, or observed dynamically, and furthermore has not been studied us-

ing SANS, especially with the use of D_2O (contrast variation method) as a wetting agent. The use of D_2O provides for improved contrast so as to understand, in detail, the absorption process that these different types of fibres undergo when dry and wet.

An outline of a long version of the SANS facility at Necsa is also discussed. Modelling and implementation of this version is also presented. This completed facility will be used to study various characteristics of nano materials, amongst others, to determine the conformation of polymers, the molecular constituents of biological molecules, the critical opalescence at second order phase transformations, etc. These very different examples demonstrate the broad field of applications using SANS technique.

Preface

The work presented here is divided into seven chapters as outlined below:

Chapter 1 presents the motivation of the study.

Chapter 2 presents a literature review of the scattering process in the context of the Small Angle Neutron Scattering (SANS) technique. The process is similar to that for X-rays (SAXS).

Chapter 3 outlines the work carried out to realise the SANS system at Necsca. Also, results using a standard sample to validate the design, as well as the recommendations to achieve a state-of-the-art SANS facility are presented. The chapter concludes in mentioning some of the examples obtained from the literature on SANS applications.

Chapter 4 summarises the literature concerning wool and mohair fibres of relevance to the SANS and SAXS techniques.

Chapter 5 presents the small-angle scattering (SAS) experiments undertaken in studying different wet and dry wool fibres as well as the results.

Chapter 6 discusses the overall results of wool fibres obtained by SANS

and compares with those obtained by SAXS and from the literature.

Chapter 7 presents an overall summary and conclusion of the work as well as the recommendations required to realise the state-of-the-art SANS facility at Necsca.

Some of this work was presented locally in the form of oral (2009) and poster (2012) presentations at the South African Institute of Physics (SAIP) Conference. It has also been presented as a poster at the 5th European Conference on Neutron Scattering (ECNS5) in Prague, Czech Republic (2011). Through IAEA and Necsca funding, the work has also been presented at the neutron scattering schools at Helmholtz-Zentrum Berlin in Germany, and Dynamics and Kinetics Neutron School in ANSTO, Lucas Heights – Australia, both in year 2010.

Contents

Title	i
Declaration	iii
Acknowledgements	vi
Abstract	ix
Preface	xii
List of Figures	xx
List of Tables	xxii
1 Introduction	1
1.1 Motivation	1
1.2 Scope of the work	2
2 Scattering Overview	4
2.1 Introduction	4
2.2 Basic properties of neutrons	5

<i>CONTENTS</i>	xiv
2.3 Sources of neutrons	10
2.3.1 Continuous nuclear reactors	11
2.3.2 Pulsed Reactors	12
2.3.3 Spallation Neutron Sources (SNS)	13
2.4 Neutron-matter interaction	14
2.4.1 Neutron scattering wave function	15
2.4.2 Neutron Cross Sections and Scattering Lengths	20
2.4.3 Coherent and incoherent scattering cross-sections	25
2.5 Neutron Scattering Instruments	27
2.5.1 Elastic Scattering	27
2.5.2 Inelastic Scattering	28
2.6 SANS Instrumentation	29
2.7 Calibration standard	30
2.8 Complementary Technique	31
2.8.1 Introduction	31
2.8.2 The Theory of SAXS	31
2.8.3 Characteristic of SAXS instrument used	32
3 SANS Characterization	34
3.1 Components installation and testing	34
3.1.1 Cryostat and filters	35
3.1.2 The Neutron Velocity Selector (NVS)	36
3.1.3 Monitor Counter	38
3.1.4 Collimation (Flight path)	39
3.1.5 The Sample Environment	39

<i>CONTENTS</i>	xv
3.1.6 Scattering Chamber	40
3.1.7 The Detection System	41
3.1.8 Beam Stop	42
3.1.9 Data Acquisition System	43
3.1.10 Data Treatment for SANS	44
3.2 Characterization by silver behenate	45
3.2.1 Aim	45
3.2.2 Procedure	45
3.2.3 Results	48
3.2.4 Discussions	50
3.3 Modelling of Phase 2	53
3.3.1 Aim	54
3.3.2 Procedure	55
3.3.3 Results	56
3.3.4 Discussions	59
4 Literature Review of Wool	60
4.1 Introduction	60
4.2 Physical structure of wool fibres	64
4.3 Chemical structure of wool fibres	67
5 Experiments	74
5.1 Introduction	74
5.2 SANS	75
5.2.1 Introduction	75
5.2.2 Aim	75

<i>CONTENTS</i>	xvi
5.2.3 Procedure	75
5.2.4 Results	76
5.2.5 Discussion	78
5.3 SAXS	79
5.3.1 Aim	79
5.3.2 Procedure	79
5.3.3 Results	79
6 Results and Discussions	81
6.1 Introduction	81
6.2 Study of Wool Fibres	81
6.2.1 SANS	81
6.2.2 SAXS	85
6.3 Discussion	86
6.4 SANS Applications	89
7 Conclusions	92
7.1 Summary of the work	92
7.2 Recommendations	93
Bibliography	99

List of Figures

2.1	Small-angle scattering set-up (neutrons or X-rays)	5
2.2	Scattering interaction of neutrons, X-rays and electrons	7
2.3	Scattering cross section as a function of atomic mass.	9
2.4	Nuclear fission process.	12
2.5	Spallation nuclear reaction process	14
2.6	Scattering between incident beam of neutrons and a fixed target: the scattered neutrons are detected within a solid angle $d\Omega$ along the (θ, φ) direction	17
2.7	The distance \mathbf{r} from the target to the detector is too large compared to the size \mathbf{r}_j of the target: $\mathbf{r} \gg \mathbf{r}_j$	18
2.8	Geometry for scattering experiment	21
2.9	Schematic representation of an elastic neutron scattering method.	28
2.10	Schematic representation of an inelastic neutron scattering method.	29
2.11	Schematic representation of a small angle neutron scattering instrument.	30

3.1	Short version of SANS instrument installed at SAFARI-1 Research Reactor showing the cryogenic filters, the neutron velocity selector (NVS), the collimator, the samples space and the scattering chamber (artistic impression).	35
3.2	Neutron flux as a function of temperature.	36
3.3	Dependence of the wavelength of neutrons transmitted by the rotor of the velocity selector on its rotation speed. The solid curve corresponds to the calculation as provided by the supplier.	37
3.4	Side view of a scattering chamber used for SANS at Necsa.	41
3.5	54 ³ He Position Sensitive Detectors as installed at the Necsa SANS facility. A B ₄ C beam stop is situated in front of the detectors. The electronics box is housed immediately behind the detectors	42
3.6	Mesytec data acquisition system. Left (MPSD-8): the amplifier module for 8 detectors. Right (MCPD): central processing unit with Ethernet output	43
3.7	Necsa's DAQ system showing only three MPSD-8 with detector tubes connected, MCPD-2 and a data acquisition control computer	44
3.8	Spectrum from silver behenate obtained from BNC SANS facility. The speed of the selector was set at (a) 6000 r.m ⁻¹ and (b) 3500 r.m ⁻¹	48

LIST OF FIGURES

xix

3.9	2D spectra obtained from Necsas SANS facility: (a) Silver behenate, (b) empty cell (Al-foil), (c) water sample, (d) Empty beam transmission, (e) background and (f) cadmium.	49
3.10	2D spectra obtained after subtraction of background and associated data.	50
3.11	$I(q)$ versus q plotted from Figure 3.10 as well as the Gaussian fit to extract the corresponding q -value.	51
3.12	Proposed layout of extended SANS beam line to be installed on beam tube number 1 of the SAFARI-1 research reactor, guided by modelling and available space for installation (artistic impression).	53
3.13	Simulated Maxwellian distribution of intensity as a function of (a) energy and (b) wavelength at the end of the in-pile guide.	57
3.14	Simulated distribution of intensity as a function of (a) energy and (b) wavelength determined by the NVS parameters.	58
3.15	Simulated distribution of intensity as a function of (a) energy and (b) wavelength at the sample position with 9 m long collimation.	58
4.1	α -Helical conformation of polypeptide chain	61
4.2	β -sheet conformation of polypeptide chain	62
4.3	Schematic representation of wool fibre structure	63
4.4	Organization of ortho- and para-cortex along the wool fibre	65
4.5	Schematic representation of bonds in wool	71
4.6	Change of moisture regain of wool with humidity	72

LIST OF FIGURES

xx

5.1	SANS sample set-up of the fibres in a quartz tube stretched on both ends for alignment.	76
5.2	SANS spectra obtained for 25.5 μm diameter mohair fibres (M5), collected from BNC facility: (a.) Clean and dry, (b.) Dirty and dry, (c.) Clean and wet, and (d.) Dirty and wet.	77
5.3	Spectra showing (a.) M4, (b.) M5 and (c.) M1097 samples, respectively, both wet with 20% D_2O	78
5.4	SAXS spectra obtained from mohair fibres, collected at the Australian Synchrotron SAXS instrument.	80
6.1	Spectra from M5 wet samples (a) dirty and (b) clean. The spectra are sectorised, (a) -along the fibre and (b) -perpendicular to the fibre, for further analysis.	82
6.2	A plot of $I(q)$ versus Q for a 20% D_2O -wet wool showing short (C) and long (J) accessible sample to detector distance merged, the 3-fitting components (F4, F5 and F6) as well as their sum (F3) using equation 6.1	83
6.3	Scattered intensity as a function of Q for data sectors perpendicular to the fibres at different conditions from M5 sample.	85
6.4	Scattered intensity as a function of Q for data sectors perpendicular to the fibres that are clean and dirty, both wet with 20% D_2O from sample M1097.	86
6.5	Spectrum (a.) and a plot of a radial average for I versus q (b.) for fibre sample obtained from a AS	87

List of Tables

2.1	Basic Properties of neutrons.	6
2.2	Summary of low-energy neutron scattering lengths and cross-sections for first few elements in the periodic table	8
2.3	Thermal neutrons classification	9
2.4	Scattering lengths of nuclides	18
2.5	Instrument parameters of Australian Synchrotron SAXS instrument	33
3.1	Characteristics of the rotor of the mechanical monochromatic velocity selector at Necsca.	38
3.2	Characteristic parameters of the SANS instrument at BNC and Necsca.	52
4.1	Typical elemental composition of dry wool and human hair fibres.	68
4.2	Typical elemental composition of vegetable fibres	69
4.3	Typical elemental composition of synthetic fibres	69
4.4	Amino acid composition of fine merino wool	70
4.5	Moisture absorption and swelling of wool	73

LIST OF TABLES

xxii

6.1	Data plot and fitting of M5 wet and dry samples along the perpendicular (vertical sectors) direction of the fibres as extracted from Figure 6.3.	85
6.2	Data plot and fitting of M1097 wet sample along the perpendicular (vertical sectors) direction of the fibres as extracted from Figure 6.4.	87

Chapter 1

Introduction

Small Angle Neutron Scattering (SANS) is a non-destructive technique [1–4] where low energy neutrons directed to a sample, are scattered by the sample in a small angle ($0.2 - 20^\circ$), and the resulting collected scattering pattern is analysed to provide information about the size, shape and orientation of the components of the sample.

1.1 Motivation

The South African Nuclear Energy Corporation (Necsa) is re-establishing SANS capabilities at its 20 MW SAFARI-1 research reactor. The advantage of SANS over other small-angle scattering methods (such as small-angle X-ray or light scattering) is the deuteration method (contrast variation) which consists in using deuterium labelled components in the sample in order to enhance their contrast. This is reminiscent of contrast variation in microscopy whereby the level of light incident upon a sample is varied using a

diaphragm. SANS can measure either naturally occurring contrasts or artificial contrasts introduced through deuteration. Labelling is not possible with X-rays (SAXS) since the scattering power increases with increase in atomic number. SANS can measure density fluctuations and composition (or concentration) fluctuations, while SAXS can measure only density fluctuation. The deuteration method allows this bonus.

SANS is disadvantaged over SAXS by the intrinsically low flux of neutron sources (nuclear reactors or spallation sources using cold source moderators) compared to the orders of magnitude higher fluxes for x-ray sources (rotating anode or synchrotrons). Neutron scattering in general is sensitive to fluctuations in the density of nuclei in the sample whereas X-ray scattering is sensitive to inhomogeneities in electron densities.

On the other hand, microscopy has the advantage that data are acquired in direct (real) space whereas scattering methods (such as SANS and SAXS) measure in reciprocal space. Electron microscopy (EM) and SANS are complementary methods. EM is applied on very thin samples only, it cannot measure samples at different concentrations and temperatures directly, and the observed images are a 2D projection. SANS can do all these things but cannot produce an image in real space. Thus small angle scattering and microscopy techniques are complementary.

1.2 Scope of the work

In summary, the aim of this study was:

- To demonstrate the SANS capabilities at Necsca using standard samples,

- To apply Monte Carlo simulation code to study SANS set-up, and
- To apply the SANS technique to study wool fibres under different conditions.

The development of a SANS instrument used to study different materials (in all states) at nanometre level was carried out in two phases. The first phase was to rebuild a short radial beam line to demonstrate the capabilities of this instrument by characterising it using standard samples.

The second phase was to extend the beam line by introducing curved neutron guides and longer scattering chamber, to increase momentum transfer range and to improve the signal-to-noise ratio. Using Monte Carlo simulation, second phase was modelled with the available components to determine the usable neutron current at the sample.

Finally, the SANS technique was used to study the different types of wool fibres subjected to different conditions such as moisture and deuteration. This work attempted to provide an indication as to what structures in textile fibres are responsible for absorbing water as well as retaining it. The outcome of such studies apply to facilitating production of improved properties of textile products for public consumption.

Chapter 2

Scattering Overview

2.1 Introduction

With the advent of nuclear reactors and spallation sources, low-energy (thermal and sub-thermal) neutrons have become a valuable tool for investigating many important features of matter at nano-structural level, particularly condensed matter, engineering and bio-material samples [5–7].

In a small-angle scattering experiment (Figure 2.1), a beam of low energy neutrons is allowed to strike a target, and the neutrons that emerge in a scattered direction, from the target are observed on an area detector. From this observation one is able to study the properties of the projectile and the target as well as the forces acting between them. This is possible when one observes the energy change and/or the change in direction of the wave vector (\vec{q}), as shown in Figure 2.1.

In the following sections, the basic properties of neutrons, their sources, and different types of neutron scattering techniques are discussed.

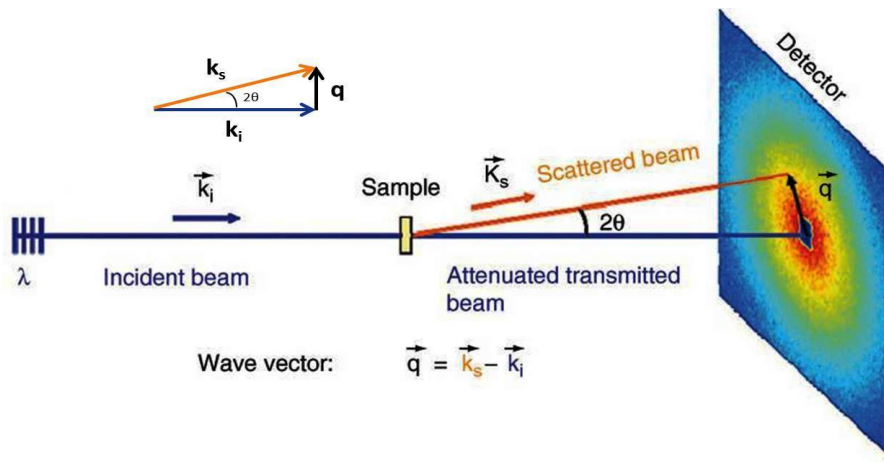


Figure 2.1: Small-angle scattering set-up (neutrons or X-rays) [8].

The behaviour of neutrons during interaction with matter is also presented. It is deemed necessary to also discuss the mathematical tools required to understand the scattering process, since the chapter would be incomplete if neutron scattering lengths and cross-sections are not discussed.

The chapter also presents the components required for a SANS set-up, standard target used in characterising these types of facilities, as well as in conclusion, summarising the complementary technique that was used.

2.2 Basic properties of neutrons

Properties of neutrons are summarised in Table 2.1 and described below as well as their advantages and disadvantages:

- Neutrons have mass which results in the de Broglie's wavelength, λ , of the slow neutrons being of the order of inter-atomic distances (few to several hundreds of nanometers) in solids and liquids. Thus, interfer-

ence effects occur which yield information about the structure.

- Neutrons interact with nuclei of the matter via coherent and incoherent scattering lengths as well as with unpaired electrons via magnetic moments, X-rays interact with matter through electromagnetic interactions with the electron cloud of atoms, and light interacts with matter through its polarizability and is sensitive to fluctuations in the index of refraction (Figure 2.2). For this reason, neutrons have high penetration (or low absorption) for most elements making neutron scattering a bulk probe.

Table 2.1: Basic Properties of neutrons.

mass (m_n)	1.675×10^{-27} kg
charge	0
spin	$1/2$
magnetic dipole moment, μ_n	$-1.913\mu_N$

- Since neutrons are uncharged, their interaction probability with the target is very small, and is due to short-ranged nuclear and magnetic forces, thus they penetrate deeply into the target.
- Neutron scattering cross-sections, σ [10] (Figure 2.3 and Table 2.2) fluctuate with the atomic number of atoms. They vary with isotopic species as well. This allows for the implementation of isotopic substitution to increase/decrease contrast.
- Neutrons have a small magnetic moment ($\mu_n = -1.913\mu_N$, where μ_N is the nuclear magneton), thus interaction with spin and orbital magnetic moments present in samples with unpaired electrons is possible. A polarized neutron beam can thus be used to investigate magnetic

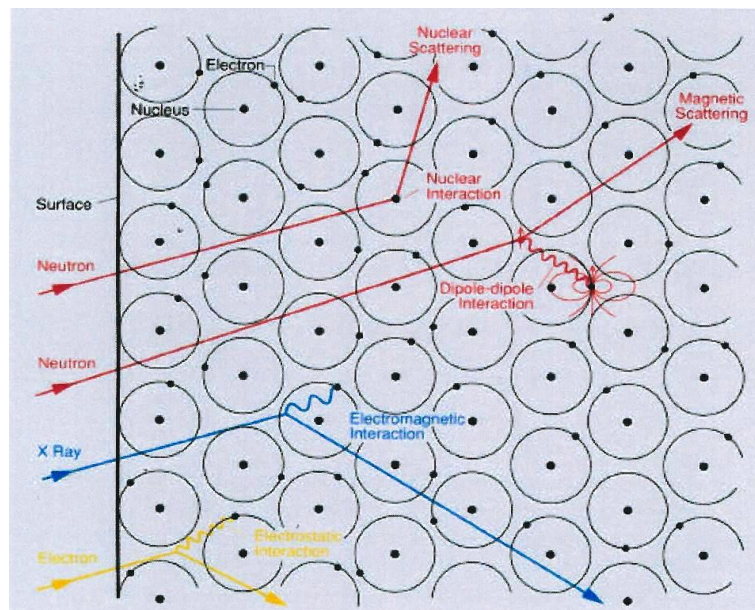


Figure 2.2: Scattering interaction of neutrons, X-rays and electrons – after [9]

phenomena directly. Elastic scattering (Section 2.5.1) from this interaction gives information on the arrangement of electron spins and the density distribution of unpaired electrons. Inelastic magnetic scattering gives the energies of magnetic excitations, and generally permits a study of time-dependent spin correlations in the scattering system.

Table 2.2: Summary of low-energy neutron scattering lengths and cross-sections for first few elements in the periodic table – after [11].

Element	Mass number	% Abundance	b^a (10^{-12}cm)	σ^b (10^{-24}cm^2)	σ_a^c (10^{-24}cm^2)
H	1	100	-0.3741	86.67	$0.3326(t^d)$
	2	0.0149	0.6674	7.63	0.000519
	3		0.494	3.03	<0.000006
He	* ^e		0.326	1.21	<0.001
	3	0.00014	0.574	5.6	$5333(t)$
	4	100	0.326	1.21	~ 0
Li	*		-0.203	1.40	70.5
	6	7.5	+0.187 -0.026i	0.98	940
	7	92.5	-0.220	1.44	0.0454
Be	9	100	0.779	7.61	0.0076
B	*		0.535 -0.021i	5.01	767
	10	20	0 -0.11i	0.98	3837
	11	80	0.666	5.8	0.006

^aCoherent scattering lengths for bound atoms. Complex values correspond to neutron wavelength of 1 Å.

^bTotal scattering cross-sections of bound atoms for thermal neutrons.

^cAbsorption cross-sections for thermal neutrons.

^dAbsorption cross-section measured with 2200 m/s neutrons.

^eNatural isotopic mixture.

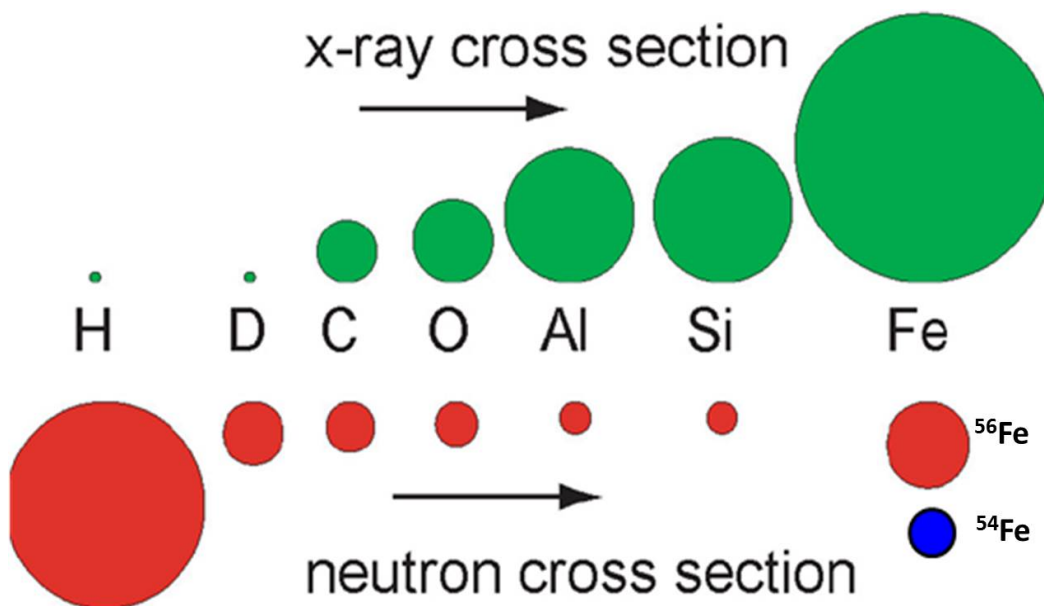


Figure 2.3: Scattering cross section as a function of atomic mass.

Table 2.3: Approximate values for the range of energy, temperature and wavelength for three types of neutron sources in a reactor –after [5].

Source	Energy (E/meV)	Temperature (T/K)	Wavelength($\lambda/\text{\AA}$)
sub-thermal (cold)	0.1 – 10	1 – 20	30 – 3
thermal	5 – 100	60 – 1000	4 – 1
epi-thermal (hot)	100 – 500	1000 – 6000	1 – 0.4

Although neutrons are good for condensed matter investigation, they also have disadvantages as listed below:

- Neutron sources are very expensive to build and to maintain. It costs millions of Rands annually to operate a nuclear research reactor and

it costs that much in electrical bills alone to run a spallation neutron source. High cost (over 2 billion dollars) was a major factor in the cancellation of the Advanced Neutron Source project in the mid 1990s [12].

- Neutron sources are characterized by relatively low fluxes compared to X-ray sources (synchrotrons) and have limited use in investigations of rapid time dependent processes.
- Relatively large amount of a sample is needed: typically 1–2 mm - thick and 1 cm diameter samples are needed for SANS measurements. This is a difficulty when using expensive deuterated samples or precious (samples that are hard to make) biology specimens (2 mm thick).

2.3 Sources of neutrons

Slow neutrons for condensed matter research are usually obtained by slowing down energetic neutrons, produced by some type of nuclear reaction, by means of inelastic collisions in a moderating material containing light atoms. The nuclear reaction of this type is obtained at reactor-based and accelerator-based facilities. Neutron sources are well described by Harron et al. [13]. These sources are based on various processes that release excess neutrons in neutron rich nuclei such as tungsten (W), uranium (U) or lead (Pb). The neutron fluxes available presently are of the order of 10^{17} n.cm⁻²s⁻¹. Even though various neutron sources exist, only a few are actually useful for scattering purposes. Neutron beams can be produced from continuous and

pulsed nuclear reactors as well as spallation sources.

Emphasis will be on continuous reactors as the SANS facilities used at Necsca and the Budapest Neutron Centre (BNC) are installed on these types of the reactors. Only minor improvements in total flux from these reactors are expected because of the saturation of the technology (i.e. limit of heat removal rate and operating safety considerations). Pulsed sources are expected to go to higher fluxes (non-continuous operations allow for a better heat removal rate). Nuclear weapons are ultimate neutron sources delivering fluxes of about 10^{26} neutrons/kiloton of explosive power in 1 μsec !, but are not practical to use for scattering purposes.

2.3.1 Continuous nuclear reactors

Continuous nuclear reactors are reactors that are based on the fission reaction of (mainly) ^{235}U to yield 2–3 neutrons/fission at around 2 MeV kinetic energy as well as photons (in the form of gamma rays) (Figure 2.4). In the reactor, the core is surrounded by a moderator, that is usually H_2O , D_2O or graphite. Neutrons produced by the core are moderated to low energies (Table 2.3). The resulting fragments are not the same element as the original atom, hence the process of transmutation occurs. The fission process is also exothermic with large amounts of energy both as electromagnetic radiation and as kinetic energy of the fragments (heating the bulk material where fission takes place) being released. For the fission process to produce energy in this case, the total binding energy of the resulting elements has to be higher than that of the starting element.

Nuclear fission produces energy for nuclear power and to drive the explosion of nuclear weapons. Both uses are made possible because certain substances called nuclear fuels undergo fission when struck by free neutrons and in turn generate neutrons when they break apart. This makes possible a self-sustaining chain reaction that releases energy at a controlled rate in a nuclear reactor or at a very rapid uncontrolled rate in a nuclear weapon.

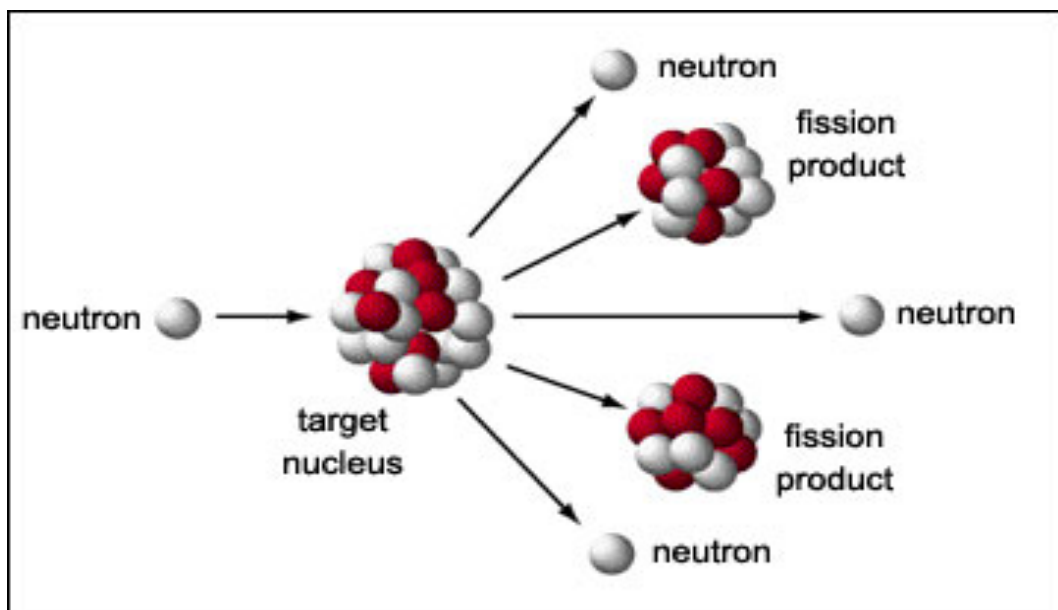


Figure 2.4: Nuclear fission process – Courtesy of <http://www.atomicarchive.com/Fission/Fission1.shtml> (accessed on 01 August 2014).

2.3.2 Pulsed Reactors

A pulsed reactor is a reactor that contains a moving element of fuel (or reflector material which periodically passes near the core), causing brief variation of the reactivity (example is IBR-II in Dubna [14]). A fast rising burst

of neutrons occurs when the reactivity exceeds prompt criticality. In this kind of reactor, average neutron fluxes are of the order of 10^{15} n.cm⁻²s⁻¹ however during the pulse (100 – 400 μ s), the number of neutrons can be as high as 10^{20} n.cm⁻²s⁻¹.

2.3.3 Spallation Neutron Sources (SNS)

Beams of high kinetic energy (typically 70 MeV) hydrogen ions are produced by linear accelerator (Linac), and an accumulator ring, which combine to produce short, powerful pulses of protons. These protons are then injected into a synchrotron ring to reach much higher energies (500 – 2000 MeV) and then steered to hit a neutron rich target (tungsten, tantalum, lead, uranium or liquid mercury) and produce about 10 - 30 neutrons/proton (see Figure 2.5) with average energy of about 1 MeV. These high energy neutrons are then moderated (by water, liquid hydrogen or methane or solid methane) before they can be used for scattering experiments. This is done in a series of moderators that surround the target assembly. Most spallation sources operate in a pulsed mode (with a repetition rate of 10 – 60 Hz). The wavelength of the neutrons can then be determined by the time-of-flight method, where time elapsed between the pulse and the neutron detection is measured. This removes the need for monochromation (required for continuous reactors) for most applications. The spallation process produces relatively few gamma rays but the spectrum is rich in high energy neutrons. Typical fast neutron fluxes are $10^{15} - 10^{16}$ n.cm⁻²s⁻¹ with a 50 MeV energy deposition per neutron produced.

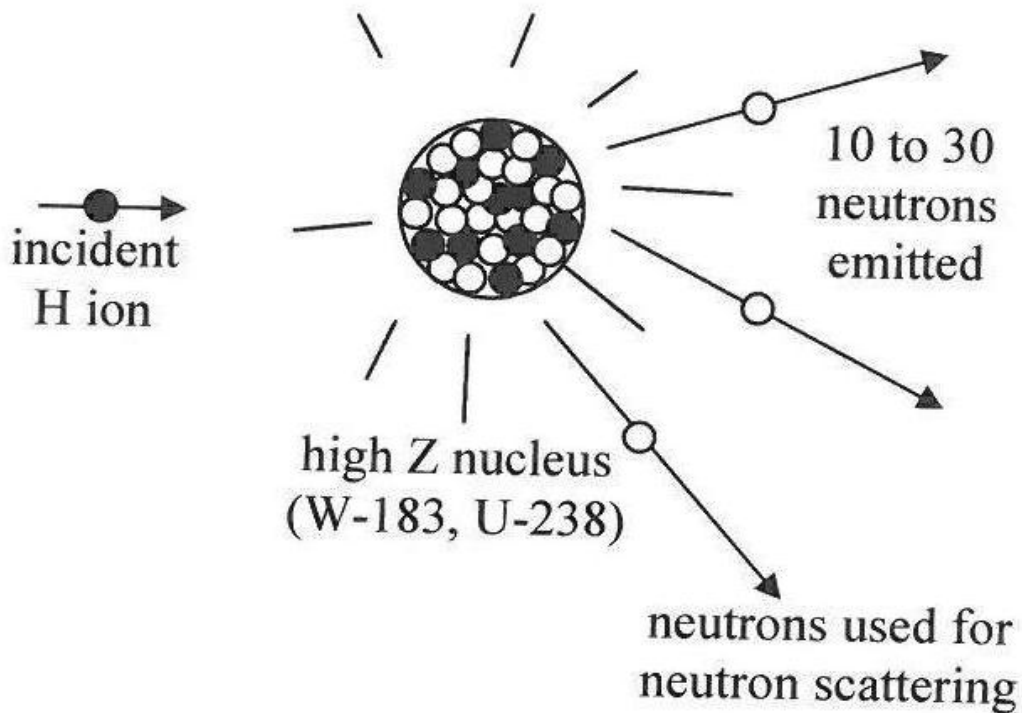


Figure 2.5: Spallation nuclear reaction process – after [15].

2.4 Neutron-matter interaction

The scattering of neutrons occurs in two ways, either through interaction with the nucleus (*nuclear scattering*) or through interaction of unpaired electrons with the magnetic moment of the neutron (*magnetic scattering*) [16, 17].

Discussion of this work will only be focussing on the former.

The scattering of a beam of neutrons from a single nucleus is considered. This is the process where the scatterer is considered fixed and there is no energy transfer between the neutron and the scatterer. The process is called elastic scattering.

The scattering process is a quantum mechanical problem even though

there are no bound states. The following section attempts to solve the scattering problem using the Schrödinger equation. Using this procedure the scattering cross section is calculated from the scattering lengths of the scatterer. This is the only way to mathematically obtain the information about the scattering experiment, thus the scattering length and the scattering cross section are also discussed in the following section. The types of scattering cross sections are also discussed although SANS involve coherent cross sections due to the fact that nuclear spins are ignored. Thus although incoherent scattering cross section is discussed, this is merely for clarity as the work does not involve investigation of magnetic scatterers.

2.4.1 Neutron scattering wave function

Figure 2.6 illustrates a scattering process. A beam of incoming neutrons (neutron flux) can be represented by a plane wave with wave-function [18, 19] as

$$\psi_i(\mathbf{z}) = \frac{1}{\sqrt{Y}} e^{i\mathbf{k}_i \cdot \mathbf{r}} \quad (2.1)$$

where \mathbf{z} is the distance from the nucleus in the direction of propagation, \mathbf{r} is the distance from the target to the detector (Figure 2.6), $k = 2\pi/\lambda$ is the wave-number and Y is a normalization constant. This implies that the density of the incoming neutron is $|\psi|^2 = \frac{1}{Y}$. It has no implication on the final results, since Y will finally leave the equations, but the normalization is kept for completeness. This is a solution of a Schrödinger equation focusing on the continuous spectrum with positive eigenvalues because, as

already mentioned, the scattering problem does not involve bound states. It is also expected that, at long distances from the origin of the potential, the solution approximates a plane wave with energy $E = \hbar^2 k^2 / 2m_n$, where \hbar is the reduced Planck's constant defined as $\hbar = h/2\pi$, where h is the Planck's constant and m_n is the mass of the neutron as indicated in Table 2.1.

From the momentum of the neutron, $\mathbf{p} = m_n \mathbf{v} = \hbar \mathbf{k}$, the velocity of a plane neutron wave packet is given

$$\mathbf{v} = \frac{\hbar \mathbf{k}}{m_n} \quad (2.2)$$

Using equations (2.1) and (2.2), the corresponding incident flux is then given by

$$\Phi_0 = v |\psi_i|^2 = \frac{1}{Y} \frac{\hbar k_i}{m_n} \quad (2.3)$$

As pointed out previously, the interaction probability is rather small and in a typical experimental situation most neutrons are transmitted without any interaction. Some, however, will be scattered and can be measured with a neutron detector placed as shown in the figure. The range of these forces are femto-metres (fm), much smaller than the neutron wavelength (which is in the order of Å). Thus, the neutron cannot probe the internal structure of the nucleus, and the scattering from a single nucleus is, by the first Born approximation [18] isotropic.

Since an idealized situation where neutrons with a well defined velocity are

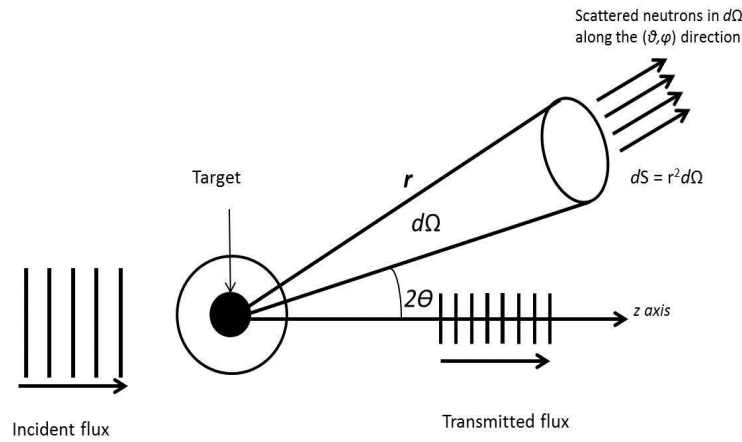


Figure 2.6: Scattering between incident beam of neutrons and a fixed target: the scattered neutrons are detected within a solid angle $d\Omega$ along the (θ, φ) direction

scattered by nuclei which are somehow fixed in position is considered, the scattered neutrons can be described as a spherical wave leaving the nuclei, which are centred at \mathbf{r}_j , as shown in Figure 2.7. The scattered wave function $\psi_f(\mathbf{r})$ is then given by

$$\psi_f(\mathbf{r}) = \psi_i(\mathbf{r}_j) \frac{-b_j}{|\mathbf{r} - \mathbf{r}_j|} \exp(ik_f|\mathbf{r} - \mathbf{r}_j|) \quad (2.4)$$

where the subscript f denotes final, b is the nuclear scattering length of the nuclei, measured in femto-metres (fm) (see Table 2.4 for examples of scattering length values). The scattering length is a measure of the strength of interaction of a neutron wave with a given nucleus of the sample. The minus sign is arbitrary and is used so that a positive value for b indicates a repulsive interaction potential. The scattering length is a complex number, but the imaginary component only becomes important for nuclei that are

highly absorptive (such as boron or cadmium) and it can otherwise be treated as a real quantity. This equation is valid only for $|\mathbf{r} - \mathbf{r}_i| \gg b$, which is always the case for a small angle scattering set-up (Figure 2.7).

Table 2.4: Values of scattering lengths

Nuclides	Combined spin	Scattering length $b(\text{fm})$
^1H	1	10.85
	0	-47.50
^2H	$3/2$	9.53
	$1/2$	0.98
^{23}Na	2	6.3
^{59}Co	1	-0.91
	4	-2.78
	3	9.91

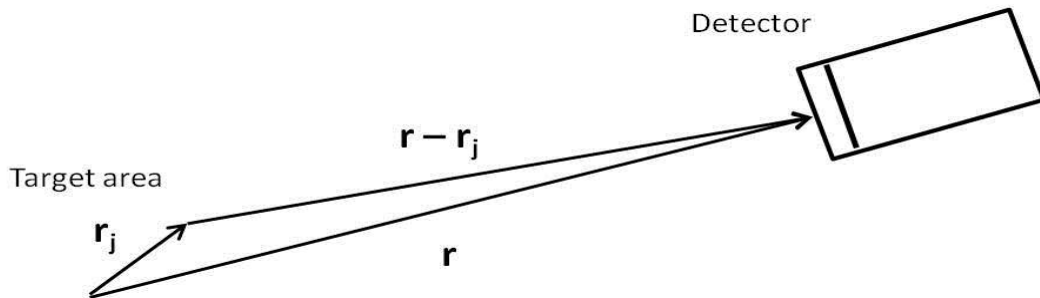


Figure 2.7: The distance \mathbf{r} from the target to the detector is too large compared to the size \mathbf{r}_j of the target: $\mathbf{r} \gg \mathbf{r}_j$.

In neutron scattering experiments, r is typically of the order 1 m or higher, while the nuclear coordinate, \mathbf{r}_j , is typically of the order of a mm or less. Hence, the density of outgoing neutrons can be approximated by $|\psi_f|^2 \approx b^2/(Yr^2)$. The number of neutrons per second intersecting a small

surface, dS , is

$$vdS|\psi|^2 = vdS\frac{b^2}{r^2} = vb^2d\Omega \quad (2.5)$$

Using Equations (2.2) and $d\Omega = \frac{dS}{r^2}$ (defined by Figure 2.6), we reach

$$\text{number of neutrons scattered per second in a solid angle } d\Omega = \frac{1}{Y} \frac{b^2 \hbar k_f}{m_n} d\Omega \quad (2.6)$$

Since the nucleus is fixed, the scattering must conserve the energy of the neutron, hence *elastic scattering*, i.e. $k_i = k_f$ (the diffraction process which is discussed in Section 2.5.1).

Again, if the incident beam is characterized by a uniform flux Φ_0 (neutrons crossing unit area per unit time), the sample has N identical atoms in the beam, and the detector subtends a solid angle $d\Omega$ and has efficiency e_{ff} , we may expect the count rate C in the detector to be proportional (if $d\Omega$ is small enough) to all these quantities. This is indeed the case, and the constant of proportionality is called the differential cross section (to be discussed in detail in the following section) and is defined by

$$\frac{d\sigma}{d\Omega} = \frac{C}{\Phi_0 N(d\Omega) e_{ff}} \quad (2.7)$$

This is the quantity that is measured in the small angle scattering. The interaction between a slow neutron and an atom through the nuclear force

can be expressed in a very simple form. To illustrate this we consider the case where the atoms in the sample are both non-interacting and identical. In this case the differential cross section is just a constant:

$$\frac{d\sigma}{d\Omega} = b^2 \quad (2.8)$$

where the scattering length b is as introduced above, and is a property only of the nucleus of the scattering atom (its atomic number Z and atomic weight A).

2.4.2 Neutron Cross Sections and Scattering Lengths

Neutron cross-section (σ) of a system is defined as an ability of the system to scatter neutrons:

$$\sigma = \frac{1}{\psi} \times \text{number of neutrons scattered per second} \quad (2.9)$$

Consider a beam of slow neutrons with energy E , incident on a target (Figure 2.8).

A target is generally a collection of atoms - being either a crystal, an amorphous solid, a liquid, or a gas. It can be generally called a scattering system. Various types of measurement can be made on the neutrons after they have interacted with the scattering system. The results in each case can be expressed in terms of a neutron cross-section (σ), which is a measure of the interaction between a neutron and a target.

A neutron counter is set-up at the end to measure the number of neut-

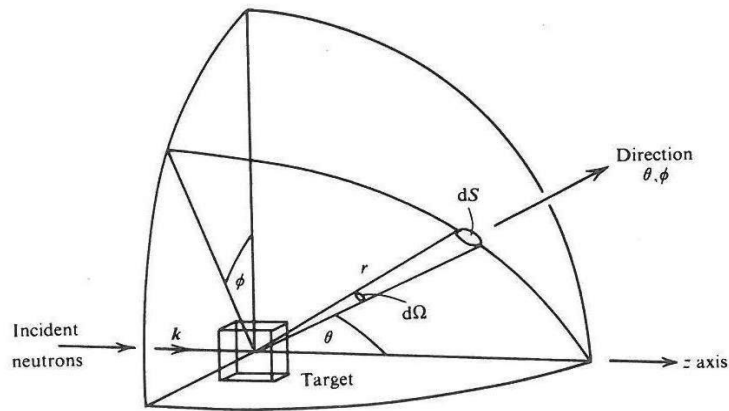


Figure 2.8: Geometry for scattering experiment – after [11].

rons in a given direction as a function of their energy E' . The distance of the counter from the target is assumed to be large (as is always the case for neutron scattering experiments (see Figure 2.7)) compared to the dimensions of the counter and the target, so the small solid angle $d\Omega$ subtended by the counter at the target is well defined. To specify the geometry of the scattering process we use polar coordinates, taking the direction of the scattered neutrons to be θ and ϕ . Using first- and second-order partial differentiation theory [20], we can define the *partial differential cross-section* as

$$\frac{d^2\sigma}{d\Omega dE'} = \frac{\text{(number of neutrons scattered per second into a small solid angle } d\Omega \text{ in the direction } \theta, \phi \text{ with final energy between } E' \text{ and } E'+dE')}{\Phi_0 d\Omega dE'} \quad (2.10)$$

The *differential cross-section* when not considering the energy of the neutron after scattering but simply counting all the neutrons scattered into the

solid angle $d\Omega$ in the direction of θ and ϕ is given by

$$\frac{d\sigma}{d\Omega} = \frac{\text{(number of neutrons scattered per second into } d\Omega \text{ in the direction of } \theta, \phi)}{\Phi_0 d\Omega} \quad (2.11)$$

And the *total scattering cross-section* where scattering is considered in all directions is defined by

$$\sigma_{tot} = \frac{\text{total number of neutrons scattered per second}}{\Phi_0} \quad (2.12)$$

Equation (2.12) is related to equation (2.11) as

$$\sigma_{tot} = \int \frac{d\sigma}{d\Omega} d\Omega \quad (2.13)$$

As mentioned earlier, the cross section is the quantity that is actually measured in a scattering experiment and the basic problem is to derive theoretical expressions that describe it for given systems of scatterers. Experimentally the cross sections are usually quoted per atom or per molecule and thus the definitions above are then divided by the number of atoms or molecules in the scattering system.

We can calculate the cross section $d\sigma/d\Omega$ for scattering from a single fixed nucleus using the expressions given above. Treating elastic scattering, the number of scattered neutrons passing through an area dA per second is given by Equation (2.5). Inserting Equations (2.2) and (2.5) into Equation (2.3),

the incident flux is simply given by the neutron velocity, that is:

$$\Phi_0 = v|\psi_i|^2 = v \quad (2.14)$$

Then from Equation (2.11), we obtain

$$\frac{d\sigma}{d\Omega} = \frac{vb^2d\Omega}{\Phi_0d\Omega} = b^2 \quad (2.15)$$

i.e. the differential cross section is a square of the scattering length. Thus if the scattering is axially symmetric, i.e. $d\sigma/d\Omega$ depends only on θ and not on ϕ , the total cross-section σ , is then given by:

$$\sigma_{tot} = 2\pi \int_0^\pi \frac{d\sigma}{d\Omega} \sin\theta d\theta \quad (2.16)$$

Equation (2.16) does not take into account the initial and final spin states of the neutron, which, as mentioned before, is beyond the study of this work.

The amplitude of neutrons scattered into an angle 2θ from a collection of objects, located by vectors \mathbf{r}_j and characterized by scattering length b_j is obtained as the sum of all scattering sites of the target, taking the phase into account:

$$f(q) = \sum b_j \cdot \exp(i\mathbf{q} \cdot \mathbf{r}_j) \quad (2.17)$$

The intensity $I(q)$ is proportional to the square of the scattering amp-

litude:

$$I(q) = K.|f(q)|^2 \quad (2.18)$$

where K is given by the geometrical configuration, the intensity of the incident flux (Equation 2.3) and the sample transmission. Normalization with respect to these parameters gives the differential cross section:

$$\frac{d\sigma}{d\Omega} = \sum \sum b(\mathbf{r}_i)b(\mathbf{r}_j).exp(i(\mathbf{q}.\mathbf{r}_{ij})) \quad (2.19)$$

where $\mathbf{r}_{ij} = (\mathbf{r}_i - \mathbf{r}_j)$. It is useful to replace the scattering length $b(\mathbf{r}_i)$ with the parameter $\eta(\mathbf{r}_i)$ describing the fluctuations from average: $\eta(\mathbf{r}_i) = b(\mathbf{r}_i) - \langle b \rangle$, and defining the correction function $\gamma_{ij} = \eta(\mathbf{r}_i)\eta(\mathbf{r}_j) / \langle \eta^2 \rangle$. Inserting of this into (2.19) gives:

$$\frac{d\sigma}{d\Omega} = \langle \eta^2 \rangle \sum \gamma_{ij}.exp(i(\mathbf{q}.\mathbf{r}_{ij})) \quad (2.20)$$

In small angle scattering experiments the resolution is not on the atomic distances. The discrete scattering lengths can therefore effectively be replaced by a continuous function, the scattering length density $\rho(\mathbf{r})$, defined as the average value:

$$\rho = \sum b_i / V \quad (2.21)$$

summed over an appropriate volume V of the sample. Equivalently, one can define a continuous fluctuation parameter η as the deviation from the

average: $\eta(\mathbf{r}) = \gamma(\mathbf{r}) - \langle \gamma \rangle$. The pre-factor $\langle \eta^2 \rangle$ in Equation (2.20) is for a two phase system with scattering length densities ρ_A and ρ_B easily shown to be equal $\rho_A - \rho_B^2 = (\Delta\rho^2)$. With the summation in Equation (2.20) replaced by the integration, one obtains for scattering differential cross-sections:

$$\frac{d\sigma}{d\Omega} = (\Delta\rho^2) \int_{\text{volume}} \rho(\mathbf{r}) \cdot \exp(i(\mathbf{q} \cdot \mathbf{r})) \quad (2.22)$$

with the integration made over the whole sample volume. Although the above discussion does not consider spin interaction between the nucleus and the neutron, if the two interact via spin interaction, the total cross-section contains both, coherent and incoherent terms.

2.4.3 Coherent and incoherent scattering cross-sections

Practically, all real systems have a distribution of both elements their isotopes, thus atomic nuclei are characterized by a coherent and an incoherent neutron scattering lengths b [13] Thus, the total cross-section (σ_{tot}) is, in fact, the sum of two components, i.e. *coherent* part and an *incoherent* part:

$$\sigma_{tot} = \sigma_{coh} + \sigma_{incoh} \quad (2.23)$$

The coherent scattering cross section, σ_{coh} , represents scattering that can produce interference and thus provides structural information. It is the scattering that the same system would give if all scattering lengths were the same as \bar{b} , the average scattering length. Although the incoherent cross sec-

tion does not give structural information, it depends only on the correlation between the positions of the same nucleus at different times. Thus, the incoherent scattering is the term added to the coherent scattering to obtain the scattering due to the actual system. The two are related to the mean and variance of the scattering length such that

$$\sigma_{coh} = 4\pi\langle b \rangle^2 \quad (2.24)$$

and

$$\sigma_{incoh} = 4\pi(\langle b^2 \rangle - \langle b \rangle^2) \quad (2.25)$$

From Equations (2.24) and (2.25), the total scattering cross section is

$$\sigma_s = 4\pi\langle b^2 \rangle \quad (2.26)$$

It was previously discussed that the scattering length b is, in fact, a complex number. If the imaginary part, which represents the absorption, is taken into account, then the total scattering cross section becomes

$$\sigma_{tot} = \sigma_s + \sigma_a = \sigma_{coh} + \sigma_{incoh} + \sigma_a \quad (2.27)$$

where σ_a is the *absorption cross section*.

2.5 Neutron Scattering Instruments

There are two main types of neutron scattering techniques, namely, elastic and inelastic scattering techniques. These are described below.

2.5.1 Elastic Scattering

Figure 2.9 shows an elastic neutron scattering set-up. The elastic scattering process is one wherein neutrons interact with the sample without energy transfer to the nucleus of the sample, but change in direction. It consists in measuring the scattered intensity with varying scattering angle. This is a way of resolving the scattering variable

$$q = \frac{4\pi}{\lambda} \sin(\theta) \quad (2.28)$$

where λ is the neutron wavelength and 2θ is the scattering angle. This is performed by either step-scanning or using a position-sensitive detector (PSD). The main types of elastic scattering instruments are diffractometers (either for single-crystal, powder diffraction or for diffuse scattering from amorphous materials), reflectometers and SANS instruments. Diffractometers probe the high- q range ($q > 0.5 \text{ \AA}^{-1}$) whereas reflectometers and SANS instruments cover the low- q range ($q < 0.5 \text{ \AA}^{-1}$). They all investigate sample structures either in crystalline or amorphous states.

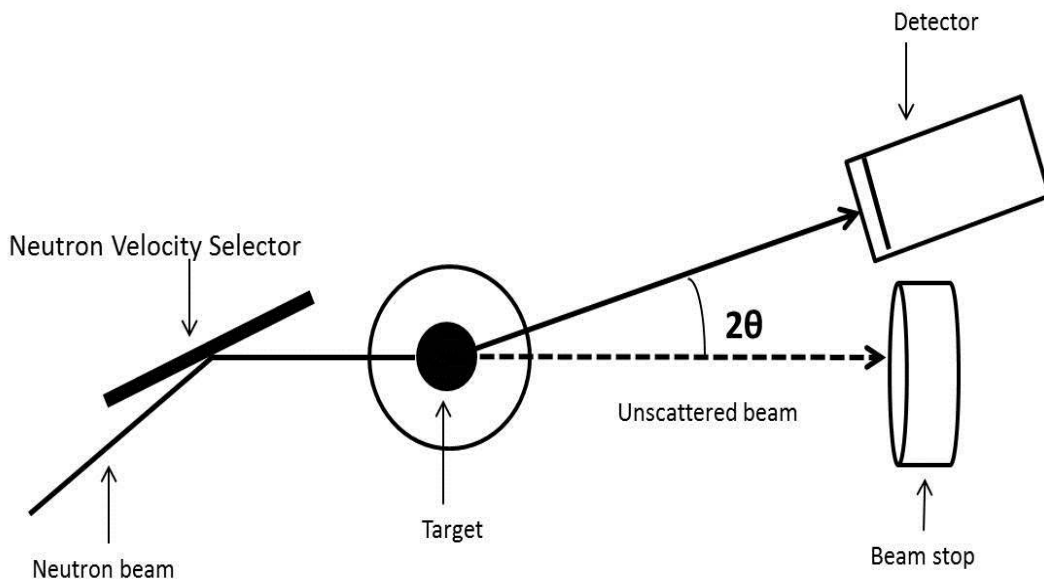


Figure 2.9: Schematic representation of an elastic neutron scattering method.

2.5.2 Inelastic Scattering

Figure 2.10 shows an inelastic neutron scattering set-up. The inelastic (or quasi-elastic) process is one wherein neutrons after interacting with matter, not only change direction, but also lose or gain energy. It consists in monochromation, collimation, scattering from a sample, analysis of the neutron energies and detection. The extra step uses a crystal analyser (or the time-of flight method) in order to resolve the energy transfer during scattering. In this case both $q = k_s - k_i$ and $E = E_s - E_i$ are resolved, where k_i and k_s are incident and scattered wave vectors, respectively, and E_i and E_s are incident and scattered energies of the projectile, respectively. Quasi-elastic scattering corresponds to energy transfers around zero, whereas inelastic scattering corresponds to finite energy transfers. The main types of quasi-elastic/inelastic

spectrometers are the triple axis, the time-of-flight, and the backscattering spectrometers. These instruments cover the μeV to meV energy range. They investigate sample dynamics and structure. Inelastic instruments are used to investigate phonon optics and other types of normal modes, whereas quasi-elastic instruments are used mostly to investigate diffusive modes [11].

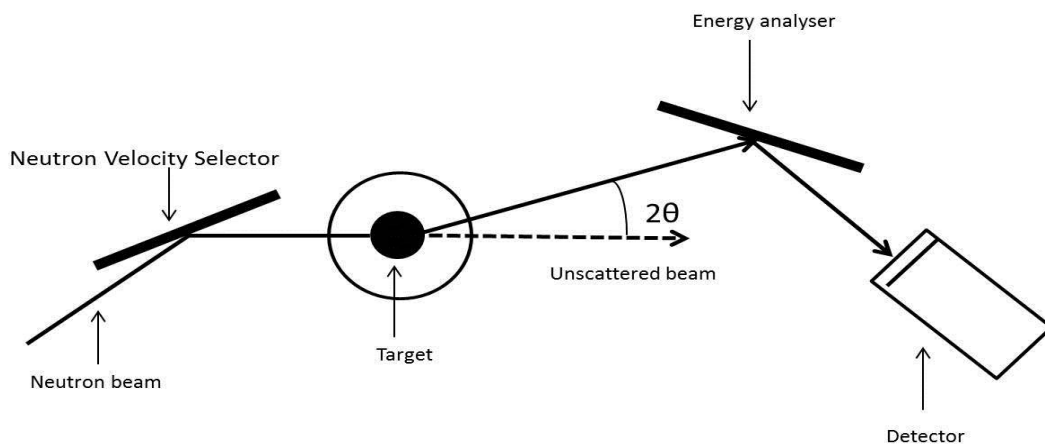


Figure 2.10: Schematic representation of an inelastic neutron scattering method.

2.6 SANS Instrumentation

Figure 2.11 shows a set-up of a small-angle neutron scattering instrument. It is in essence rather simple, consisting generally of the following primary components depending on the neutron source: cold moderator (or cryogenic filters (F in the figure)), neutron velocity selector (NVS in the figure), curved neutron guides, different lengths of pre-sample collimation, sample environment, post-sample collimation and the scattering chamber (tank) for the scattered beam housing neutron detectors. Inside the scattering chamber,

there are also small beam stops to stop the unscattered beam. In addition to these components, there are also electronics for data acquisition and software for data treatment. The primary mentioned components, except the scattering, are also buried inside the shielding, either for biological shielding or suppression of the noise into the sensitive detectors.

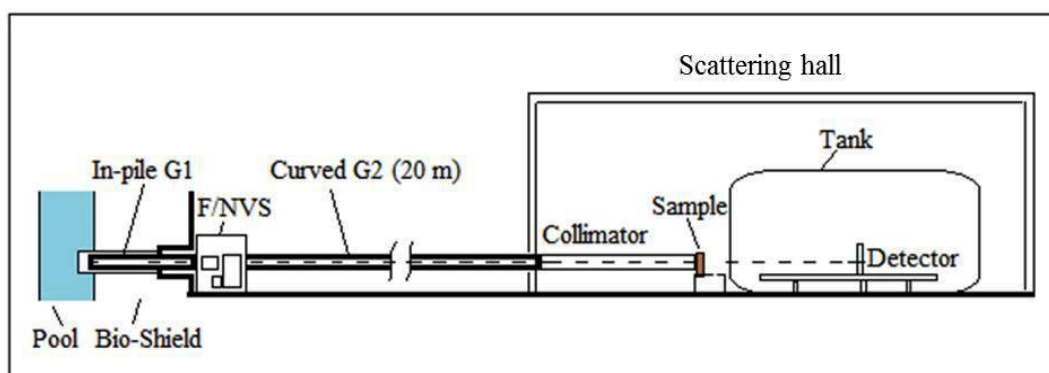


Figure 2.11: Schematic representation of a small angle neutron scattering instrument.

2.7 Calibration standard

Silver Behenate ($\text{AgC}_{22}\text{H}_{43}\text{O}_2$) is a silver salt of a long carboxylic acid [21, 22]. It has a large number of well defined diffraction (001) peaks and a known average crystallite size along the long-spacing direction, thus making it a good reference material for powder diffractometer angle calibrations in the small angle region [23].

Small-angle scattering (SAS) calibrants are used to accurately determine the sample-to-detector distance, which allows one to compute q (reciprocal-

space lengths) for the image on the area detector [24]. The essential criteria for any good calibrant are good reproducibility among samples, reasonably strong (intense) scattering, an appropriate length scale, and several orders of diffraction (a well-ordered sample).

2.8 Complementary Technique

2.8.1 Introduction

Although neutrons are powerful with their behaviour in impinging through the sample, they do not give all the information regarding the sample, hence it is required that studies of the sample be done and verified by other techniques such as Small Angle X-ray Scattering (SAXS).

Scattering of X-rays is a process whereby X-rays scatter primarily from electrons bound to the atoms of the sample. Due to this electromagnetic radiation, the detected scattering pattern is characteristic of the nanostructures and can be used to determine their size, shape, internal structure and more [25].

2.8.2 The Theory of SAXS

As already highlighted in Section 2.5.1, small-angle scattering (SAS) experiments generally follow the same procedure as shown in Figure 2.1, i.e. a sample is irradiated with a well-collimated beam of some type of radiation (x-rays, neutrons or light), the resulting intensity is measured as a function of angle between the incoming beam and scattered beam, then the struc-

ture that caused the observed pattern is determined. Scattering patterns are caused by the interference of secondary waves that are emitted from various structures (electrons for x-rays and light, or nuclei for neutrons) when irradiated. Scattering of x-rays is caused by differences in electron density, scattering of neutrons is caused by differences in scattering power of different nuclei and scattering of light is caused by differences in refractive index. Since the larger the diffraction angle the smaller the length scale probed, wide angle x-ray scattering (WAXS) is used to determine crystal structure on the atomic length scale while small-angle x-ray scattering (SAXS) or small-angle neutron scattering (SANS) is used to explore micro-structure on the colloidal length scale. Light is used similarly but because the wavelength of light is much greater than that of x-rays or neutrons, light scattering is used for much larger structures like the phases in blends of elastomers or particle size distributions.

As shown in eq. 2.28, there is an inverse relationship between the size of a scattering center and the scattering angle, since $q \propto 1/d$, where d is the probed length scales ranging from 10 Å to nearly 10,000 Å, for samples with well-ordered structures (crystalline structures) studied by diffraction methods (wide-angle scattering).

2.8.3 Characteristic of SAXS instrument used

Characteristic parameters for instrument used are given in Table 2.5. A pin-hole collimation was used for the measurements.

Table 2.5: Instrument parameters of Australian Synchrotron SAXS instrument

X-ray source	In-vacuum undulator
Operating voltage (KeV)	5 – 21. Optimised for 8.15 and 11.00
Wavelength (λ) of radiation (nm)	$K_{max} = 0.156$
Detector	Pilatus 1M and MAR-165 CCD
Operating temperature range($^{\circ}\text{C}$)	-30 – 300
q -range (\AA^{-1})	0.0015 - 1.1 (using multiple camera lengths)
Sample-detector distance (mm)	500 – 7000
Sample dimension (mm^3)	Samples of dimension 20 x 7 x 0.3

Chapter 3

SANS Characterization

Instruments for SANS have been developed [1–4] at many international research reactors and most spallation sources, and gained a lot of popularity due to their special applications in studying materials at very small length scales.

The following sections discuss the SANS facility set-up, the characterization of the facility using a standard sample in comparison with measurements made at another facility (Yellow Submarine). The future SANS facility design, guided by the modelling so as to implement neutron guides and longer scattering chamber, is also presented.

3.1 Components installation and testing

The layout of a short-version of the SANS facility at Necsca is shown in Figure 3.1. The components of this facility are individually described below with their tested characteristics.

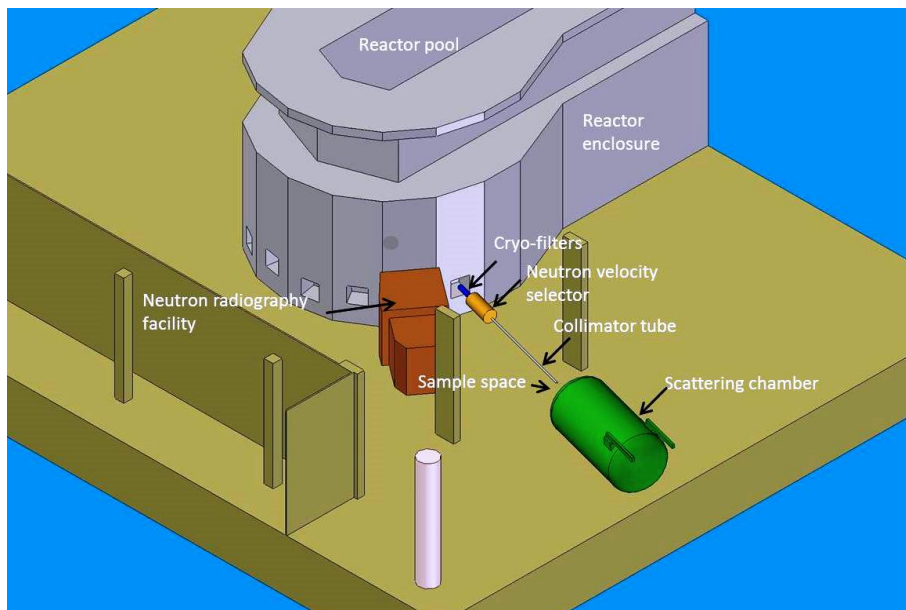


Figure 3.1: Short version of SANS instrument installed at SAFARI-1 Research Reactor showing the cryogenic filters, the neutron velocity selector (NVS), the collimator, the samples space and the scattering chamber (artistic impression).

3.1.1 Cryostat and filters

At the end of the reactor biological shielding (Figure 3.1) lies a cryostat housing single-crystal Beryllium (20 cm) and Bismuth (20 cm) filters. They are cryogenically cooled down to 70 K and below to remove fast neutrons and γ -rays as well as to improve the transmission of the thermal and sub-thermal neutrons with wavelengths above 4 Å with 90 % transmission. Figure 3.2 shows a plot of neutron transmission flux as a function of filter temperature. The operation of the cryogenic system is not included in this section, but

interested readers may obtain the information from <http://www.janis.com/> (accessed on 01 August 2014).

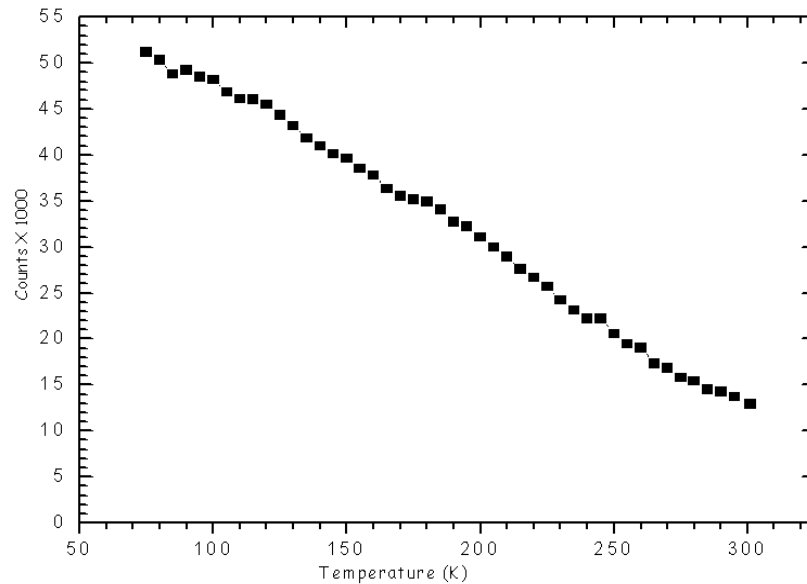


Figure 3.2: Neutron flux as a function of temperature.

3.1.2 The Neutron Velocity Selector (NVS)

The NVS was installed with a mechanism of raising and lowering, but no tilting. The latter capability is provided in the design for the NVS installation in Phase 2. Calibration of the NVS in a 0° tilt angle was provided by the supplier (Figure 3.3, the solid line) [26]. This plot was produced using the following equation:

$$\lambda = A/\omega \quad (3.1)$$

where λ (\AA) is the wavelength of the transmitted neutrons, ω (rpm) is the rotational speed of the rotor, and $A = 1.2 \times 10^3$ is a constant determined by the rotor design parameters. The experimental data obtained during calibration (Figure 3.3, the \bullet on the graph) fit the calculations well. The NVS parameters are given in Table 3.1. Of interest is the operating speed of 3000 rpm (corresponding to the wavelength of 4.16 \AA as shown in Figure 3.3) due to filter cut-off of the usable beam above this speed (Section 3.1.1).

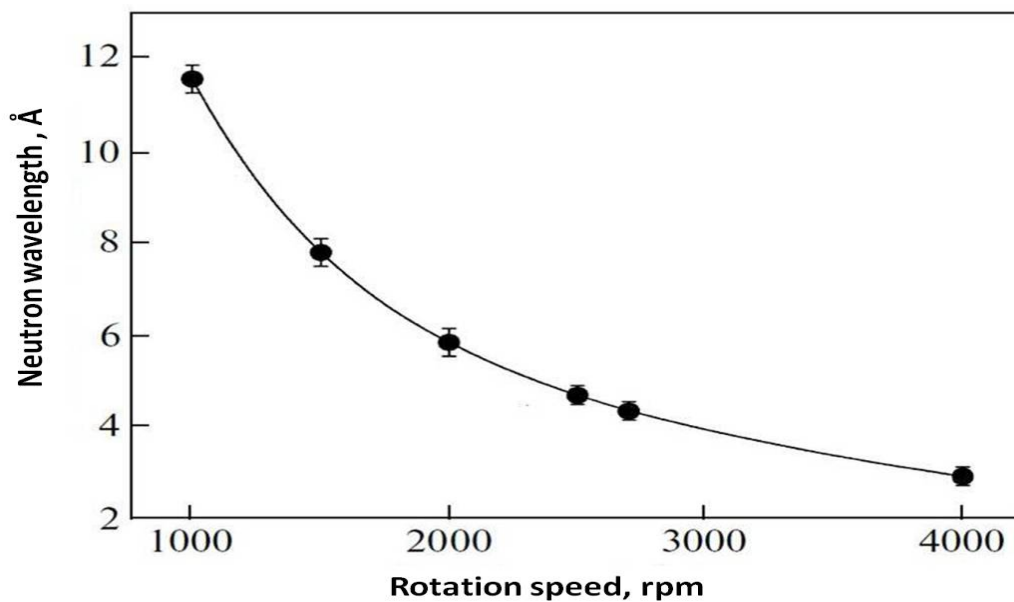


Figure 3.3: Dependence of the wavelength of neutrons transmitted by the rotor of the velocity selector on its rotation speed. The solid curve corresponds to the calculation as provided by the supplier.

Table 3.1: Characteristics of the rotor of the mechanical monochromatic velocity selector at Necsca.

Characteristic	Value
Effective length	650 mm
Diameter corresponding to the slit half-height	420 mm
Slit height	60 mm
Slit width at half-height	5.5 mm
Angular rotation of the slit in the effective length	12°
Divergence angle	0.5°
Thickness of the absorbing plates	0.5 mm
Transmittance of useful neutrons	~75%
Range of operating rotating speed	1000 – 4500 min ⁻¹
Range of separated neutron wavelengths	3 – 10 Å
Transmittance of the rotor	~75%
Neutron wavelength resolution ($\frac{\Delta\lambda}{\lambda}$)	~15%
Weight of the rotor	~50 kg

3.1.3 Monitor Counter

Between the velocity selector and the pre-sample collimation system, a low-efficiency fission chamber detector (the size of a pencil not shown in Figure 3.1) is used to monitor the neutron beam during data acquisition.

3.1.4 Collimation (Flight path)

The flight path is placed at the end of the neutron velocity selector. It is made of a variable length collimation (1 – 2.5 m) long mild steel pipes with 50 mm inner diameter evacuated to about 10^{-1} mbar to minimise scattering from air. The collimator is blanked on both sides by 1 mm thick aluminium flanges with minimal neutron intensity loss. To achieve a required collimation, cadmium of different slot diameter sizes from 1 – 10 mm are placed at both ends of the flight path for a particular collimation requirements. The collimator is wrapped around with B_4C flexible sheets (B_4C coated silicon) to reduce background from entering the flight path and radiation leaking out of the collimator due to neutron absorption/scattering/interaction with collimator walls.

Necsa has recently acquired a set of straight and curved neutron guides that will be installed when a longer facility is implemented (Section 3.3).

3.1.5 The Sample Environment

Although there is no sample stage currently installed, there are no complications in making sample preparation and installation. In most of our experiments, a retort-stand, an aluminium foil and a vial were sufficient to accommodate the samples. The flexibility with this set-up is that the whole sample stage can be completely withdrawn from the beam line. The insertion of the sample can be easily done away from the beam. Then sample stage can be installed back onto the beam line. Alignment is easily achieved since samples are normally 10 mm or greater in diameter, while the collimation is

10 mm or less and the samples are placed right against the collimator.

3.1.6 Scattering Chamber

A ~ 5 m long and ~ 2.5 m diameter scattering chamber is shown in Figure 3.4. As highlighted in Section 2.6, it is made of stainless steel with the primary aim of housing a detector array and its peripherals. Its interior is lined with B_4C /silicone sheets. The chamber is normally evacuated to minimise air that might contribute in the scattering recorded on the detectors, but this was never achieved as the proper feed-throughs were not acquired during operation, but they will be implemented in the second phase. Electronics modules (see Section 3.1.9 below) used for data acquisition are housed in an aluminium box located at the back of the detector array. For cooling of the electronics the interior of the box has to be in atmosphere, thus feed-throughs were used to maintain the vacuum in the chamber and atmosphere in the box. Flexible hoses were used to run air, power, heat sensors and high voltage cables into the box. They also link the central processing device to the computer by Ethernet cable. Airflow is generated by a portable blower through the hoses on one side of the box (and the scattering chamber) and extracted on the other side of the box (and the scattering chamber), such that only room temperature air is circulated in the box, and warm air is removed out of the box.



Figure 3.4: Side view of a scattering chamber used for SANS at NeCSA.

3.1.7 The Detection System

There is an array of 54 X 600 mm long (10 mm diameter) position sensitive detectors (Figure 3.5) located in the scattering chamber that are in operation. The sample-detector distance of 200 – 400 cm is achieved (in X-direction) by translation of this array inside the chamber. The array has the ability to move in Y-Z direction, as shown in the figure, thus making the alignment with the beam to the centre of the array easy.



Figure 3.5: 54 ^3He Position Sensitive Detectors as installed at the Ncsa SANS facility. A B_4C beam stop is situated in front of the detectors. The electronics box is housed immediately behind the detectors

3.1.8 Beam Stop

In front of the detector array lie 3 discs of B_4C sheets with different diameter sizes (one disk shown in Figure 3.5 in front of the array) to stop the direct beam transmitted through the sample from saturating the detectors. The beam stop movements are only fixed with respect to the X-movement of the array. They can collectively be moved in the Z-direction, but independently moved in the Y-direction, so as to select the right beam stop for a particular sample-detector distance.

3.1.9 Data Acquisition System

A fully functional complete readout system for the array of position sensitive neutron detector tubes (MESYTEC PSD) is in place. This modular system provides amplifier/converter modules, an intelligent central processing device for system control, histogramming and network interfacing, as well as the data acquisition software running on a linux system (Figures 3.6 and 3.7). This chain of electronics is installed in the aluminium box (electronics box) at the back of the detector array to avoid extensive use of vacuum feed-throughs.



Figure 3.6: Mesytec data acquisition system. Left (MPSD-8): the amplifier module for 8 detectors. Right (MCPD): central processing unit with Ethernet output. Courtesy of <http://www.mesytec.com/> (accessed on 23 May 2014).

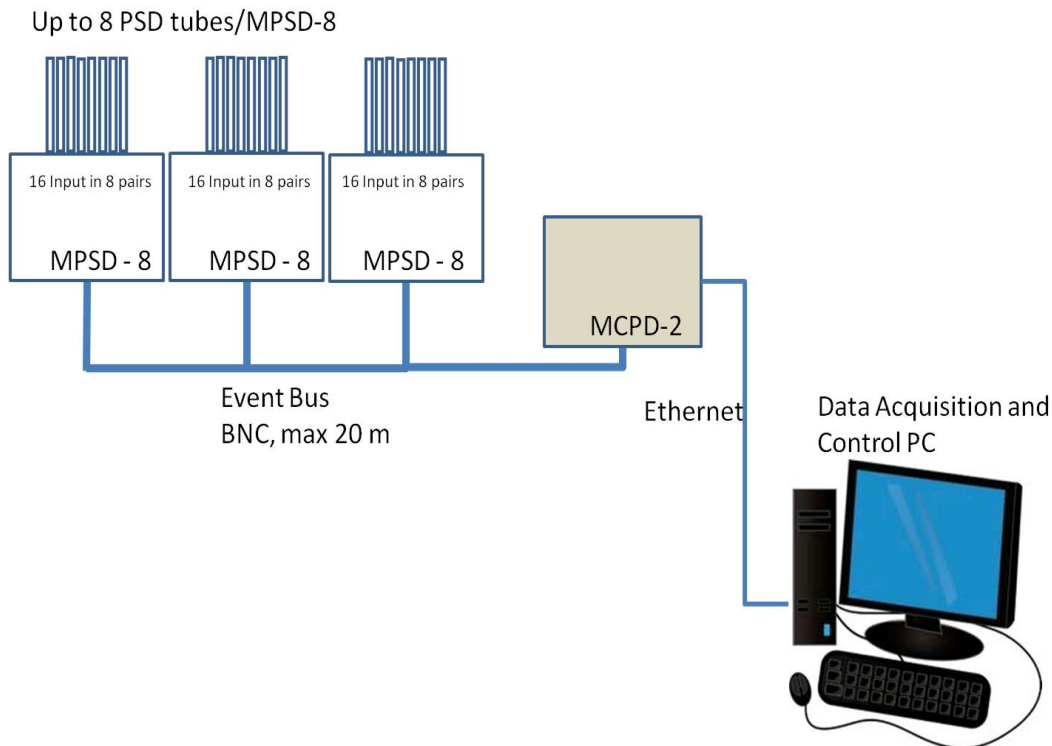


Figure 3.7: Necea's DAQ system showing only three MPSD-8 with detector tubes connected, MCPD-2 and a data acquisition control computer .

3.1.10 Data Treatment for SANS

This is the most important part of the SANS exercise. Some of the software types used in data treatment are available commercially [27] as well as freely downloadable from the web [28–30]. SANS data were reduced using freely available $GRAS_{ans}P$ [28], while SAXS data were reduced using freely available Fit2D [29], respectively. The reduced data can then be handled in any mathematical package for further analysis. In this case OriginPro package (www.originlab.com accessed on 01 August 2014) was used.

3.2 Characterization by silver behenate

This section discusses the experiments performed to characterize the SANS facility at Necsca in comparison to that done at a similar facility in Budapest Neutron Centre (Yellow Submarine SANS). Measurement procedures, i.e. sample preparation, data acquisition, data treatment and discussion are presented.

Characterization experiments carried out on the Yellow Submarine SANS were done in the range of momentum transfer $q = 0.002\text{-}0.350 \text{ \AA}^{-1}$, with neutron wavelengths λ of 4.12 \AA and 16 \AA as given by eq. 2.28. They were also carried out at the short-version of the Necsca SANS with a wavelength of about 4.16 \AA (3000 rpm NVS). Operational parameters of the two instruments will also be compared.

3.2.1 Aim

To calibrate and demonstrate the SANS capabilities at NECSA by using a standard sample (AgBeh) as well as comparing with that obtained from Yellow Submarine.

3.2.2 Procedure

- Yellow Submarine – A 1 mm thick sample of AgBeh powder mounted within a Hellma precision cell (<http://www.hellma.com/> accessed on 01 August 2014) (with wall thickness of 1.25 mm) was analysed at the BNC SANS beam line at NVS speeds of 6000, 5500, 4500 and 3500 rpm corresponding to neutron wavelengths of 4.12, 4.48, 5.43 and 6.94

Å respectively, as defined by earlier calibrations by the time-of-flight technique [31]. A similar procedure was followed for a water sample (with known scattering cross-section) and an empty holder. Hellma precision cells are favoured as they are virtually transparent to neutrons, thus the attenuation is very minimal. Transmission measurements for the sample and the cell were also made by placing a thin perspex glass along the direct beam to attenuate the beam current impinging on the detector to avoid detector saturation. This process was performed for only a minute. Background measurements were done with the beam completely stopped. A beam profile monitor was used to monitor the beam so as to make data normalisation possible. Spectra were then collected onto the computer for analysis. The data in both cases were recorded in an event-by-event basis.

- SASANS – Silver behenate powder samples were wrapped in an aluminium foil. The thickness of the foil was 0.5 mm. The foil is then mounted on a retort stand. Neutrons with definite wavelength were selected by the NVS (Section 3.1.2), collimated through to the sample to impinge the sample for an hour. Neutrons scattered by the sample were then recorded on the area detector (Section 3.1.7). Water, cadmium and empty cell measurements were also made to provide absolute calibration. Aluminium has similar properties as those of Hellma precision cell for neutrons.

Calculation of the corrected scattered intensity requires knowledge of the transmission of the sample and sample holder in order to correctly subtract

the background contributions, as shown below. T_s and T_e refer to the transmission of the sample alone and the transmission of the empty cell, respectively. The corrected scattered intensity, $I_{corrected}$ depends on the transmission values T_s and T_e and is given by:

$$I_{corrected} = \frac{1}{T_s T_e} (I_s - I_{Cd}) - \frac{1}{T_e} (I_{Bck} - I_{Cd}) \quad (3.2)$$

where I_s , I_{Cd} and I_{Bck} are, respectively the intensities of the sample, Cadmium and empty cell.

Transmissions of the sample, T_s is calculated by comparing the transmitted beam through the sample and the cell relative to the total counts for the empty cell as follows:

$$T_s = \frac{\text{Transmitted Neutrons through Sample and Cell}}{\text{Transmitted Neutrons through Empty Cell (or Holder)}} \quad (3.3)$$

Whereas the empty cell transmission, T_e , can be calculated by comparison of the transmitted beam through the empty cell, relative to the total counts in the empty beam (no cell present):

$$T_e = \frac{\text{Transmitted Neutrons through Empty Cell}}{\text{Transmitted Neutrons in the Empty Beam}} \quad (3.4)$$

Using Equation 3.2, and known scattering cross section of water (also known as the calibration standard), the scattering cross section of the sample under investigation is obtained by a simple division of the intensities meas-

ured in each pixel, multiplied by the measured scattering of water as:

$$\frac{d\sigma_{Sample}}{d\Omega} = \frac{I_{Sample}}{I_{calibration}} \times \frac{d\sigma_{calibration}}{d\Omega} \quad (3.5)$$

which simplifies Equation 2.22.

3.2.3 Results

Figure 3.8 illustrates typical 2-D intensity distributions observed at 6000 and 3500 r.m^{-1} , respectively after subtracting all other contributions using Equation 3.2.

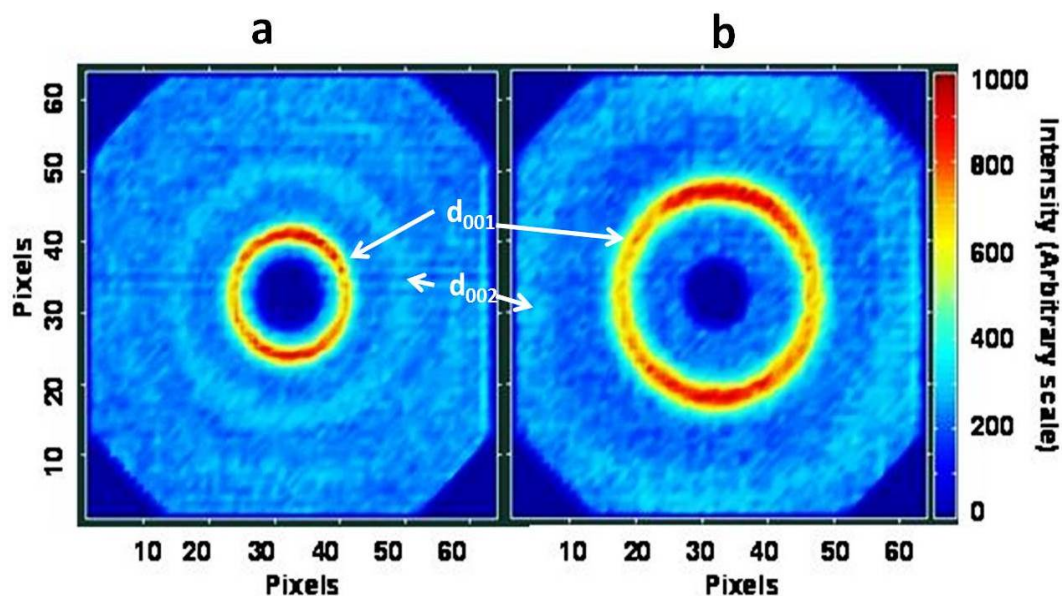


Figure 3.8: Spectrum from silver behenate obtained from BNC SANS facility. The speed of the selector was set at (a) 6000 r.m^{-1} and (b) 3500 r.m^{-1} .

Figure 3.9 show a 2D-spectra of (a) silver behenate in an aluminium foil, (b) empty aluminium foil, (c) water in an aluminium foil, (d) no sample (empty beam), (e) no beam and (f) cadmium in the beam, respectively obtained from Necsas SANS.

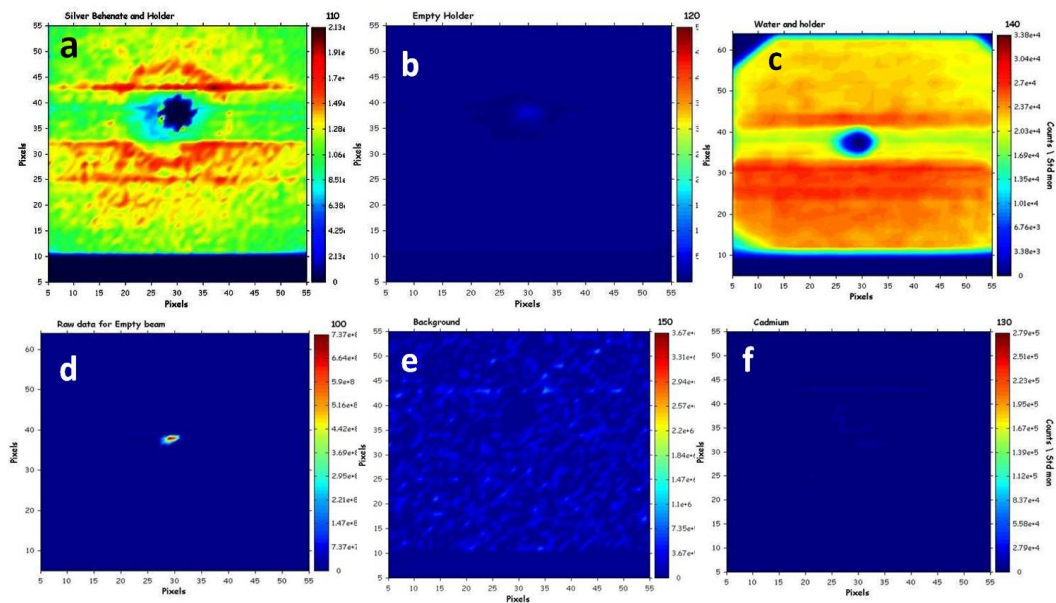


Figure 3.9: 2D spectra obtained from Necsas SANS facility: (a) Silver behenate, (b) empty cell (Al-foil), (c) water sample, (d) Empty beam transmission, (e) background and (f) cadmium.

After subtracting all other contributions, Figure 3.10 shows a 2D-spectrum of the sample with single ring clearly visible. Figure 3.11 shows a plot of intensity ($I_{corrected}$) as a function of q and a Gaussian fit to extract the q -value corresponding to the observed single ring. The results are discussed below.

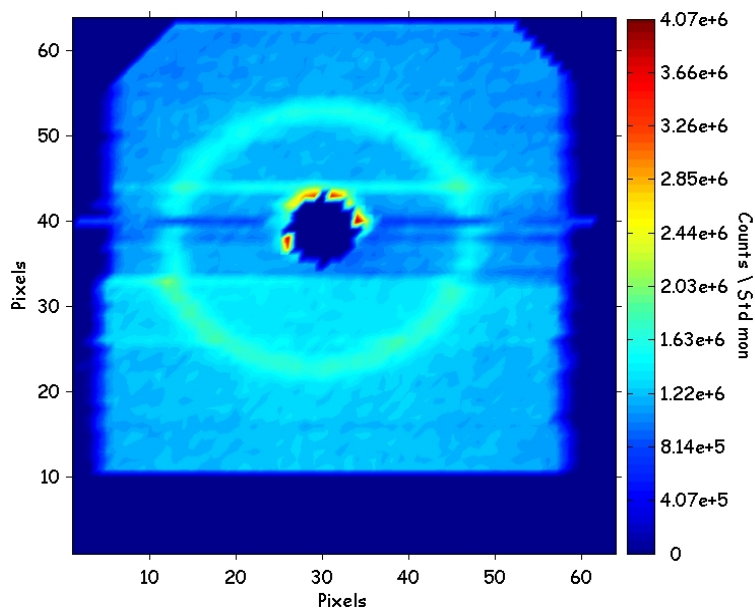


Figure 3.10: 2D spectra obtained after subtraction of background and associated data.

3.2.4 Discussions

From Figure 3.8, d_{001} and d_{002} diffraction peaks are clearly visibly separated rings.

Comparing the results obtained in both instruments, Figures 3.8b. and 3.10 clearly show d_{001} diffraction peaks. The extra ring (d_{002} peak) in Figure 3.8b) is due to the wavelength used for the set-up, which cannot be accessible in the Necsca set-up due to the Beryllium wavelength cut-off. Using GRASP, Figure 3.11 presents a plot of intensity versus q , where the Gaussian fit was used to obtain $q = 0.182 \pm 0.003 \text{ \AA}^{-1}$ corresponding to d_{001} diffraction peak. This particular q -value falls well within the general experimental SANS

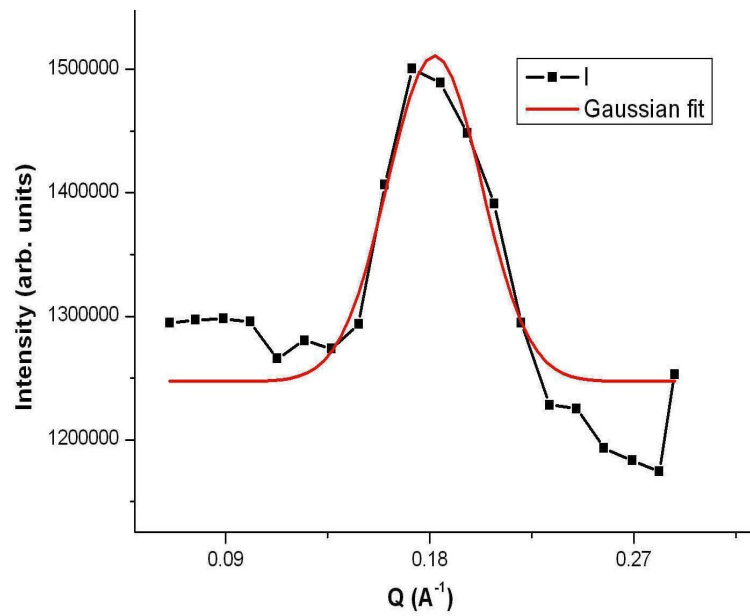


Figure 3.11: $I(q)$ versus q plotted from Figure 3.10 as well as the Gaussian fit to extract the corresponding q -value.

q -range as shown in Table 3.2. It is also the lowest sample-detector distance accessible.

Table 3.2: Characteristic parameters of the SANS instrument at BNC and Necsca.

Parameter	BNC	Necsca
Monochromator	Mechanical velocity selector	Mechanical velocity selector
Incident wavelength	3 – 25 Å	3 – ~10 Å
Wavelength spread	Adjustable between 12 - 30%	~15%
Maximum beam size at sample	16 mm diameter	40 mm diameter
Transferred momentum (q) range	0.003 – 0.5 Å ⁻¹	≤0.182 Å ⁻¹
Neutron flux at the guide exit	5 × 10 ⁷ n.cm ⁻² s ⁻¹	10 ⁶ n.cm ⁻² s ⁻¹
Sample-to-detector distance range	0.9 – 5.5 m	1.8 – 2.4 m
Detector	2-D multi-detector, 64 x 64 cm ² , filled with BF ₃ gas	2-D PSD, 54 x 60 cm ² , filled with ³ He gas
Sample environments	Thermostated sample changer, electromagnet, cryostat and furnace	Thermostated sample changer

The longer sample-to-detector distance (lower q -limits) in the Necsca set-up could not be achieved as the evacuation of the chamber was not implemented, resulting in degradation of the signal to noise ratio due to neutrons scatter in air. The evacuation of the chamber will be implemented in the

second phase for which the modelling performed is discussed in the following section.

3.3 Modelling of Phase 2

Figure 3.12 shows a longer version of the SANS facility with envisaged components. The facility will consist of an in-pile neutron guide section (currently installed), the filters, the neutron velocity selector (NVS), neutron guide curved sections and a possible straight part with decreasing geometry in order to achieve maximum neutron flux at sample position. The guide is Ni-coated to enhance the containment of the neutron intensity.

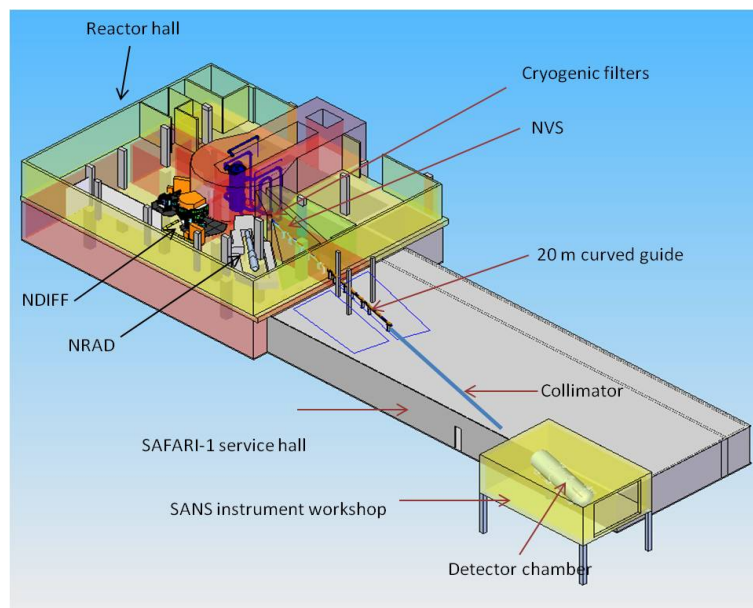


Figure 3.12: Proposed layout of extended SANS beam line to be installed on beam tube number 1 of the SAFARI-1 research reactor, guided by modelling and available space for installation (artistic impression).

To achieve maximum neutron flux at the sample, configuration of the

set-up was modelled [32] using VITESS Monte Carlo modelling [33]. VITESS is a program that allows one to construct, virtually, a neutron scattering instrument with respect to different types of neutron sources. It allows for the calculation of the intensity resolution performance in such a way that different methodological treatments (at different types of sources) can be compared with each other realistically. This process is achieved by adequately considering the intensity losses, e.g. resulting from crystal monochromatization, the neutron guide reflectivity, and/or the attenuation rate of choppers. A virtual instrument can be composed of several VITESS modules, e.g. starting with the source module randomly generating neutrons (in terms of number, divergence, energy, time distribution, place) which are taken as input for further modules describing the influence of subsequent neutron optics, instrument components and the scattering characteristics of the sample itself. Due to the modular approach, the influence of each instrument component on the neutron flux (time and energy resolved) and the resolution performance can be investigated quite easily. The modelling can be freely downloadable in a user-friendly form, i.e. with graphical user interface from http://www.helmholtz-berlin.de/forschung/oe/grossgeraete/neutronenstreuung/vitess_en.html (accessed on 01 August 2014).

3.3.1 Aim

To determine usable neutron flux at sample position of Necsas SANS facility using VITESS model.

3.3.2 Procedure

The following modules with parameters in relation to Necsans SANS were used.

The assumed direction of the beam in cartesian coordinates is the x-axis.

- Source and moderator - A Maxwellian distribution continuous source module as in SAFARI-1 reactor was used. The neutron flux of 10^{13} n.cm⁻².s⁻¹ was assumed. A 12 x 12 cm² square moderator module cooled down to 50 K temperature was used. The temperature relates to that of the filters when in operation.
- Space Window - A 4 x 4 cm² aperture rectangular space window module is placed 50 cm away from the moderator module at the face of the in-pile guide module. The space assumes neutrons propagating in air, thus minimal attenuation is expected.
- In-pile neutron guide - A 2.4 m (4 x 4 cm² aperture opening on both ends) straight guide module was used. This module simulates the neutron flight path through a mirrored guide calculating the intensity loss for each reflection (with dependence of the neutron wavelength and the incident angle).
- Neutron velocity selector - A neutron velocity selector module with parameters as shown in Table 3.1 was placed.
- Space Window - Another rectangular window module with same aperture size and similar properties was placed 10 cm away from the end of the NVS.

- Curved Neutron guide - From this position starts a 20 m curved neutron guide module with 1300 m radius of curvature and the same aperture window as the in-pile guide and the space windows.
- Space Window - Another space window module was placed 20 cm from the exit aperture of the curved guide module. The 20 cm space will be used for beam stop during sample and collimation-length change.
- Collimator - A 9 m collimator module with same same curved guide entrance and exit aperture was placed at the end of the window.

In addition, VITESS offer monitor modules that can be placed anywhere between other modules to obtain information about wavelength, time, divergence or position (y-z-plane) dependent intensity or polarization distribution of the neutron output given from the previous modules. They write the intensity or average polarization according to the segmentation of the interval of interest as ASCII data to the monitor file. The data of these file can be visualised by any graphics tool. The monitor modules do not influence the neutron stream to the following modules.

3.3.3 Results

Figure 3.13 shows a plot of simulated intensity as a function of the (a) energy and (b) wavelength (\AA) from the Maxwellian distribution at the end of the in-pile guide assuming a cold moderator at 50 K. The assumption is based on the filters used in this beam line. Figure 3.14 shows simulated intensity as a function of the energy and the wavelength at the end of the NVS rotating

at 3000 rpm corresponding to the wavelength of 4.12 Å and 15 % wavelength spread ($\Delta\lambda/\lambda$). Figure 3.15 shows the simulated intensity at the sample position after a 20 m curved guide and a 9 m collimation. This is the worst case of the set-up, although a 4 cm diameter collimation is used. The results will be discussed below.

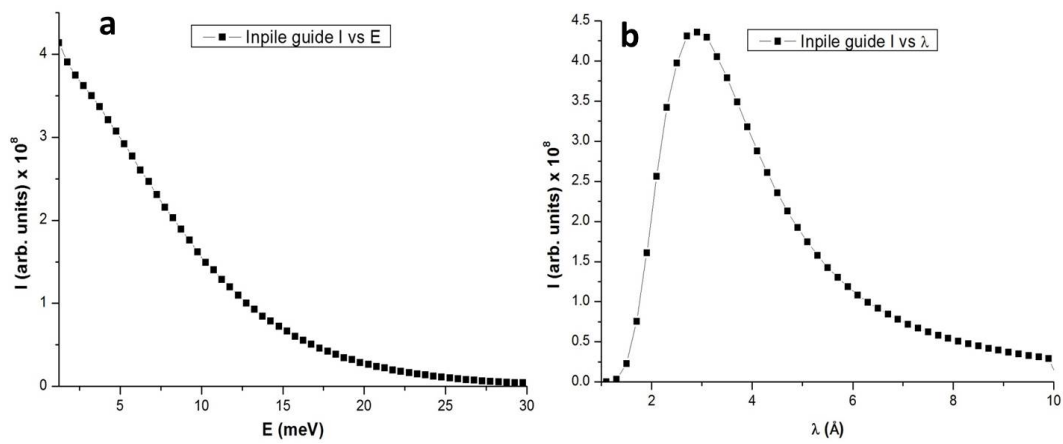


Figure 3.13: Simulated Maxwellian distribution of intensity as a function of (a) energy and (b) wavelength at the end of the in-pile guide.

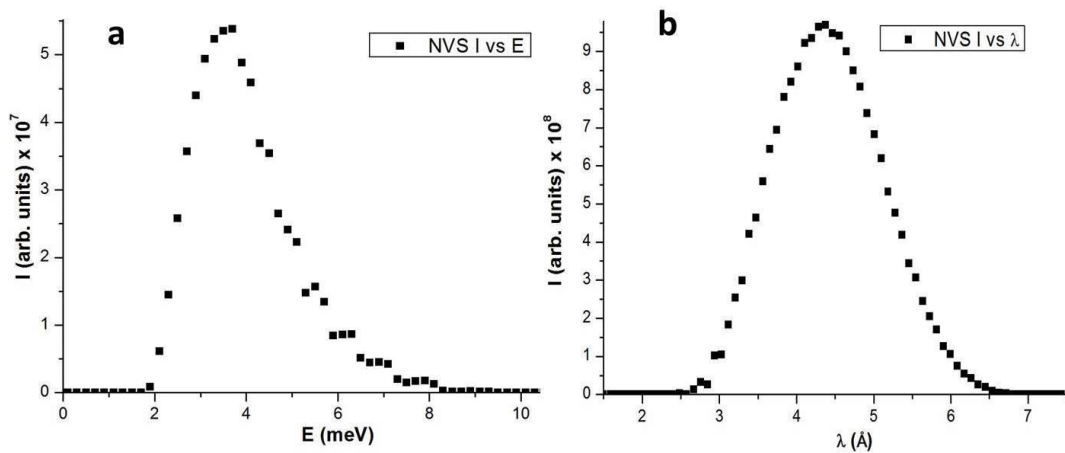


Figure 3.14: Simulated distribution of intensity as a function of (a) energy and (b) wavelength determined by the NVS parameters.

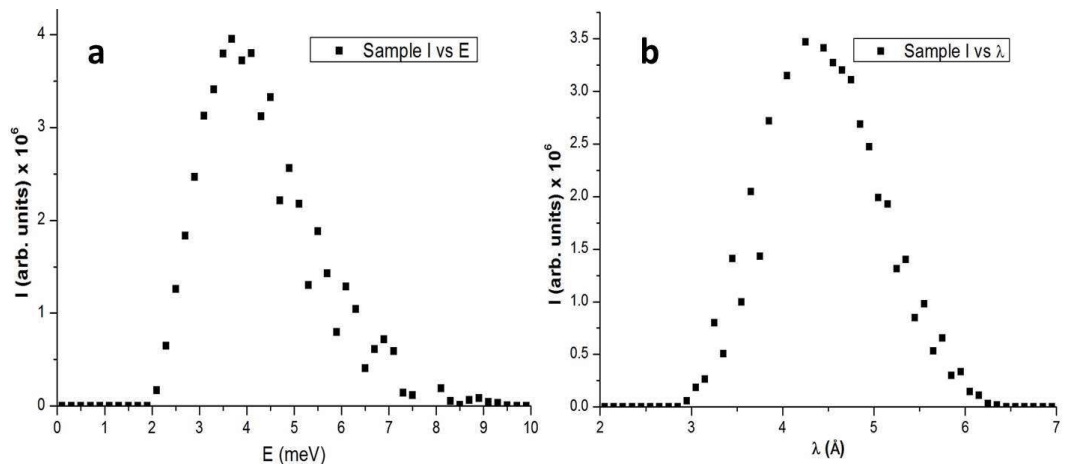


Figure 3.15: Simulated distribution of intensity as a function of (a) energy and (b) wavelength at the sample position with 9 m long collimation.

3.3.4 Discussions

From Figure 3.13, it is clearly visible that a Maxwellian distribution of the cold neutron intensity will be achieved and contained through an NVS with a defined wavelength (Figure 3.14) peaking at around 4 Å as the set-up suggests. The selected neutron intensity then travels through a 20 m long neutron guide with radius of curvature of 1300 m and a straight 20 m collimator to the target station (Figure 3.15). The collimation in this set-up is assumed to be 4 x 4 cm². This is in line with the already available neutron guide dimensions.

Comparing the neutron intensities as a function of wavelength in (b) of Figures 3.14 and 3.15, the model shows that the neutron intensity will be reduced by a factor of 100 at the sample position. This will be slightly higher as the Be filter does not have a perfect transmission, however with 10 to 100 times losses due to this implementation, i.e. $\sim 10^4$ neutrons.cm⁻².s⁻¹ at a specific wavelength, the integral flux will be considerably higher making it possible to perform SANS experiments as shown by Török [32].

It is also worth noting that the source-sample distance of 9 m is the worst case for the set-up, however the short source-sample distance (~ 2 m) will require a narrow aperture for better resolution.

Chapter 4

Literature Review of Wool

4.1 Introduction

Wool is the generally accepted generic description of the hair of various breeds of domestic sheep, although it is also commonly used as a generic name of all animal hair, particularly including the so-called fine animal hair, i.e. the hair of cashmere and angora (mohair) goat as well as the cross-breeds of both (cashgora), of camel, vicuna, alpaca, of the angora rabbit, and of many others including the hair of the yak [34, 35]. The morphology and composition of human hair also closely resembles that of wool [36].

Wool is a protein fibre and thus contains α -keratins (protein molecules in α -helix conformation, in a complex mixture with proteins of irregular structure (Figure 4.1)) [37], while silk and feathers are composed of β -keratin (protein molecules partially in β -pleated sheet conformation (Figure 4.2)).

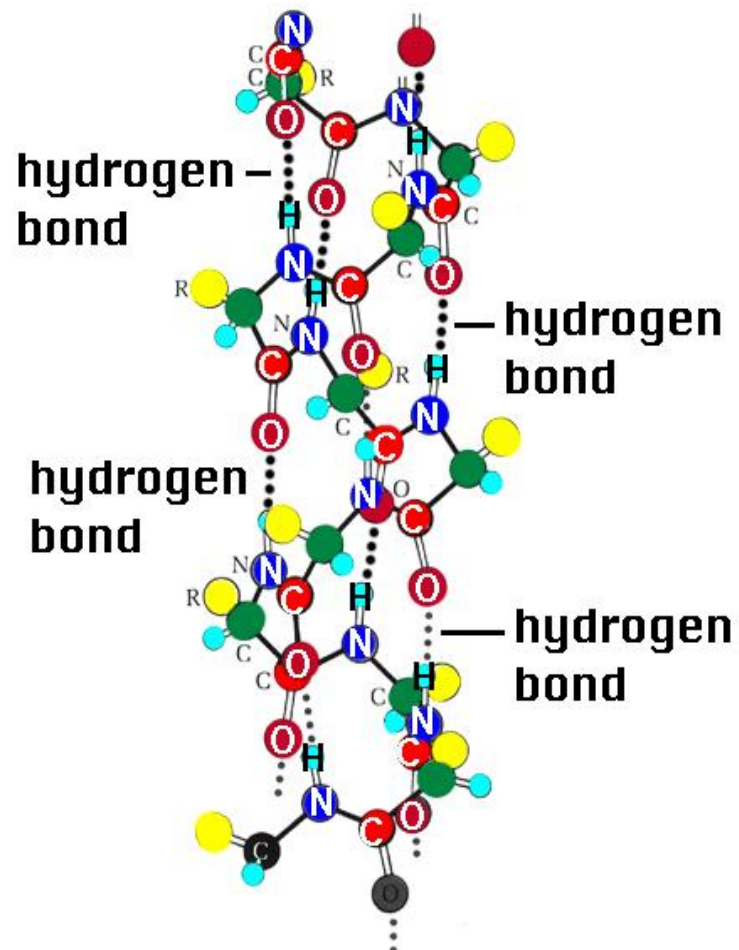


Figure 4.1: α -Helical conformation of polypeptide chain – After [34]

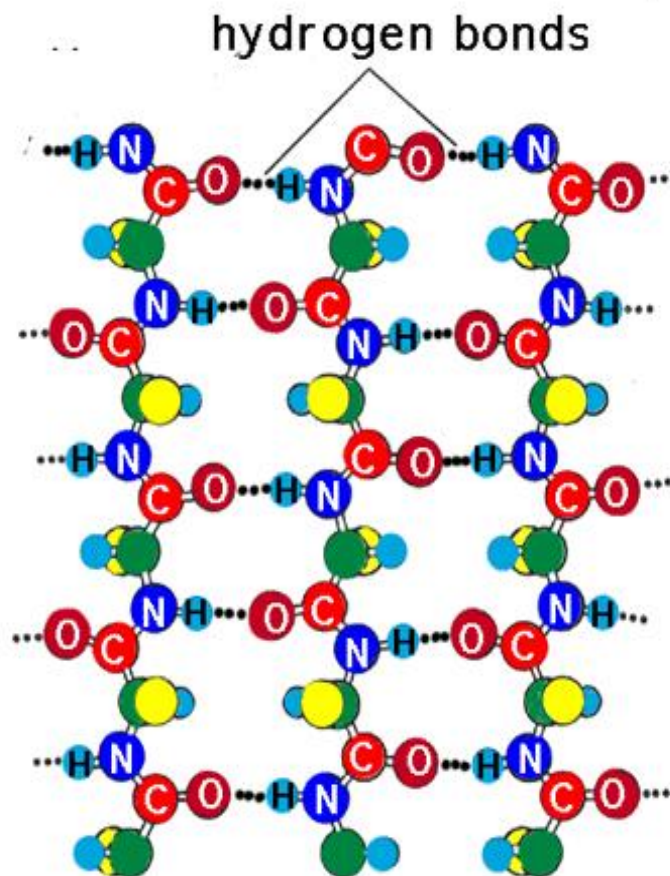


Figure 4.2: β -sheet conformation of polypeptide chain. After [34]

From a macromolecular point of view, wool is a composite fibre, i.e. a fibril-reinforced matrix material with both the fibrils and the matrix consisting of polypeptides, interconnected physically and chemically.

From a morphological point of view, wool is a nanocomposite (the reinforcing microfibrils have a diameter of about 10 nm (Figure 4.3)) of high complexity

with clear hierarchy indicating an enormous degree of self-organisation. From a protein structural point of view, only the fibrils are regarded as α -keratins, they being embedded into a protein matrix of irregular structural conformation. The microfibrils are typical intermediate filaments, i.e. one type of protein constituting the cytoskeleton, others being actin filaments and microtubuli. They are generally called keratin-intermediate filaments (or KIF) and the matrix materials in which they are embedded are called keratin associated proteins (or KAP).

Physical and chemical structures of wool fibres are described in details below.

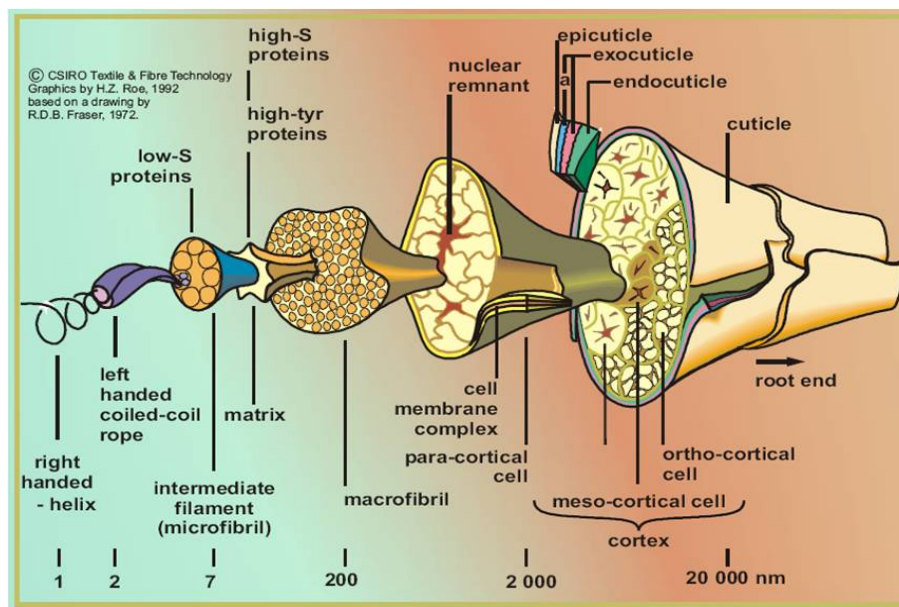


Figure 4.3: Schematic representation of wool fibre structure – Courtesy of <http://www.csiropedia.csiro.au/pages/viewpage.action?pageId=426494> (accessed on 01 August 2014).

4.2 Physical structure of wool fibres

Figure 4.3 shows the classical morphology of wool where gross hierarchy of morphological elements are shown. The fibre is composed of the following major components:

- Cuticle – On the outside of the wool fibre is a protective layer of scales called cuticle cells. The cuticle is nearly a rectangular sheet in shape, slightly bent, with a width of about 20 μm , a length of 30 μm , and a thickness of 0.5 - 0.8 μm (at the edges). These cuticles overlap like tiles on a roof. The exposed edges of the cells face away from the root end so there is more friction when you rub the fibre in one direction than the other. This helps wool expel dirt and gives it the ability to felt. Wool felts when fibres are aligned in opposite directions and they become entangled.

The scales have a waxy coating chemically bound to the surface. This stops water from penetrating the fibre but allows absorption of water vapour. It also makes wool water-repellent and resistant to water-based stains.

- Cortex – Cortex are internal cells that make up 90% of the fibre. There are two main types of cortical cells, namely ortho-cortical (60 - 90%) and para-cortical (40 - 10%), of which the latter contains a larger amount of sulphur than the former and hence being tougher and more highly cross-linked. Moreover, in fibres from fine wool breeds such as merino sheep, the two different cortex cells are arranged in a bilateral manner and the borderline between ortho- and para-cortex

proceeds in a helical manner along the fibre axis. This results in a stable crimp as the cells expand differently when they absorb moisture, making the fibre bend, with the para-cortex always situated in the inner part and the ortho-cortex in the outer part of the curvature as shown in Figure 4.4. In coarser fibres, the para-cortical and ortho-cortical cells form more randomly so there is less crimp.

Fibre crimp makes wool feel springy and provides insulation by trapping air.

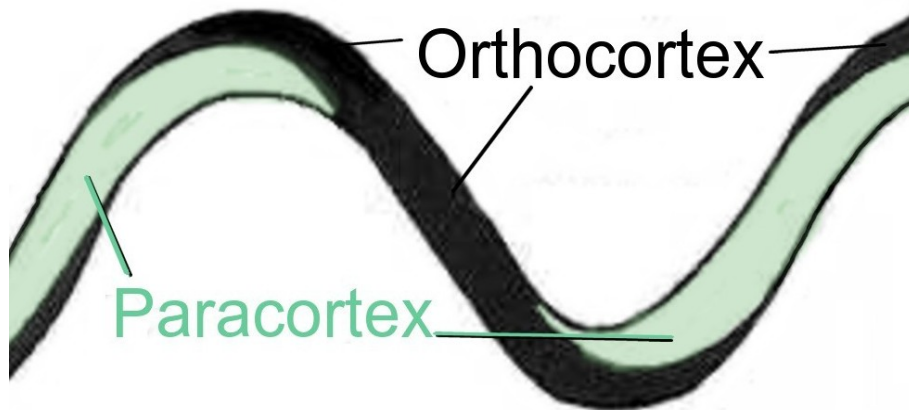


Figure 4.4: Organization of ortho- and para-cortex along the wool fibre – Courtesy of <http://www.csiropedia.csiro.au/pages/viewpage.action?pageId=426494> (accessed on 01 August 2014).

- Cortical cell – The cortical cells are surrounded and held together by a cell membrane complex, acting similarly to mortar holding bricks together in a wall.

The cell membrane complex contains proteins and waxy lipids and runs

through the whole fibre. The molecules in this region have fairly weak intermolecular bonds, which can break down when exposed to continued abrasion and strong chemicals.

The cell membrane complex allows easy uptake of dye molecules.

- Macrofibril – Inside the cortical cells are long filaments called macrofibrils. These are made up of bundles of even finer filaments called microfibrils, which are surrounded by a matrix region.
- Matrix – The matrix consists of high sulphur proteins. This makes wool absorbent because sulphur atoms attract water molecules. Wool can absorb up to 30% of its weight in water and can also absorb and retain large amounts of dye. This region is also responsible for wools fire-resistance and anti-static properties.
- Microfibril – Within the matrix area, there are embedded smaller units called microfibrils. The microfibrils in the matrix are rather like the steel rods embedded in reinforced concrete to give strength and flexibility. The microfibrils contain pairs of twisted molecular chains.
- Twisted molecular chain and helical coil – Within the twisted molecular chains are protein chains that are coiled in a helical shape much like a spring. This structure is stiffened by hydrogen bonds and disulphide bonds within the protein chain. They link each coil of the helix, helping to prevent it from stretching. The helical coil the smallest part of the fibre gives wool its flexibility, elasticity and resilience, which helps wool fabric keep its shape and remain wrinkle-free when in use.

4.3 Chemical structure of wool fibres

Wool and animal hair typically are considered as a protein fibre, thus consist of the elements such as carbon, hydrogen, nitrogen, oxygen and sulphur [34, 36, 38] (see Table 4.1). Vegetable based textile and synthetic fibres also consist of carbon, hydrogen and nitrogen, and no oxygen and sulphur (see Table 4.2 and Table 4.3), where other is in the form of sulphur, chlorine and other trace elements. In wool, except for large sulphur content, the elemental composition is typically that of proteins. The sulphur mainly derives from the amino acid cystine, which has two sulphur atoms forming a disulphide bond, this being the most important cross-linking element of wool and the process is called keratinisation, the process by which keratin is deposited in cells and the cells become horny. These make keratin fibres insoluble in water and more stable to chemical and physical attack than other types of proteins. Individual polypeptide chains are joined together to form proteins by a variety of covalent chemical bonds, called cross-links, and non-covalent physical interactions (see Figure 4.5).

Besides cystine, 20 other amino acid residues are found in wool (see Table 4.4). They are distinguished by their side chain, which imparts a special character, being either hydrophilic (water-absorbent) or hydrophobic (water-repellent), acidic or basic. Note that, in their ionised state, a deprotonated carboxylic acid group may be regarded as basic, and a protonated amino group as acidic. From Table 4.4, it can be seen that the proportions of acidic and basic groups

are approximately the same (800 - 850 $\mu\text{mol/g}$ of each). This high content of oppositely charged side chains facilitates a second kind of cross-linking, i.e. salt-bridges between glutamate or aspartate residue and a protonated lysine or arginine residue. Salt bridges will obviously be sensitive to the pH-value of the fibre.

Another kind of cross-linking element is the isodipeptide bond between glutamic or an aspartic acid and a lysine residue. Additionally, hydrogen bonds have to be included as stabilising elements of wool, notably between amide groups but also between a variety of other hydrogen donating and accepting groups. Hydrogen bonds render wool sensitive to all kinds of hydrogen bond-breaking reagents. Absorption of water, for example, has a major effect on the physical properties of wool fibres.

Table 4.1: Typical elemental composition of dry wool and human hair fibres. After [34].

Element	Weight (%)
Carbon	50-52
Hydrogen	6.5-7.5
Oxygen	22-25
Nitrogen	16-17
Sulphur	3-4
Other	0.5

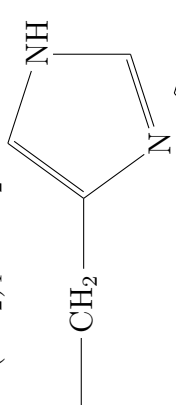
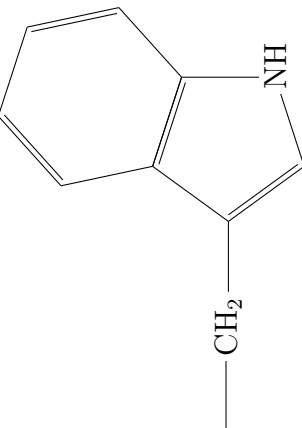
Table 4.2: Typical elemental composition of vegetable fibres. After [34]

Element	Weight (%)
Carbon	4
Hydrogen	11
Oxygen	1
Nitrogen	84
Other	0

Table 4.3: Typical elemental composition of synthetic fibres. After [34].

Element	Weight (%)
Carbon	6
Hydrogen	51
Oxygen	11
Nitrogen	32
Other	0

Table 4.4: Amino acid composition of fine merino wool. After [34]

Chemical character of side group	Name	Abbreviation	Side chain	Concentration ($\mu\text{mol}/\text{gram}$)
Amino acid and their ω -amides	Aspartic acid	D	$-\text{CH}_2-\text{COOH}$	200
	Glutamic Acid	E	$-(\text{CH}_2)_2-\text{COOH}$	600
	Asparagine	N	$-\text{CH}_2-\text{CONH}_2$	360
	Glutamine	Q	$-(\text{CH}_2)_2-\text{CONH}_2$	450
Basic amino acid and tryptophan	Arginine	R	$-(\text{CH}_2)_3-\text{NHC}(\text{NH}_2)=\text{NH}_2$	600
	Lysine	K	$-(\text{CH}_2)_4-\text{NH}_2$	250
	Histidine	H		80
	Tryptophan	W		40

Wool contains proteins of $-\text{CO} \cdot \text{NH}^-$ and other groups that attract water. Figure 4.6 depicts the change in moisture regain (i.e. mass of absorbed water/mass of dry fibre) with the relative humidity (RH). In a standard atmosphere of 65 % RH and 20°C , regain values range from 14 to 18%. Similar study was conducted by Preston and Nimkar [39], who found that loose wool retained 133% regain when centrifuged at 1000 g for 5 minutes. This contrasts with other fibres where the two methods give similar values [40].

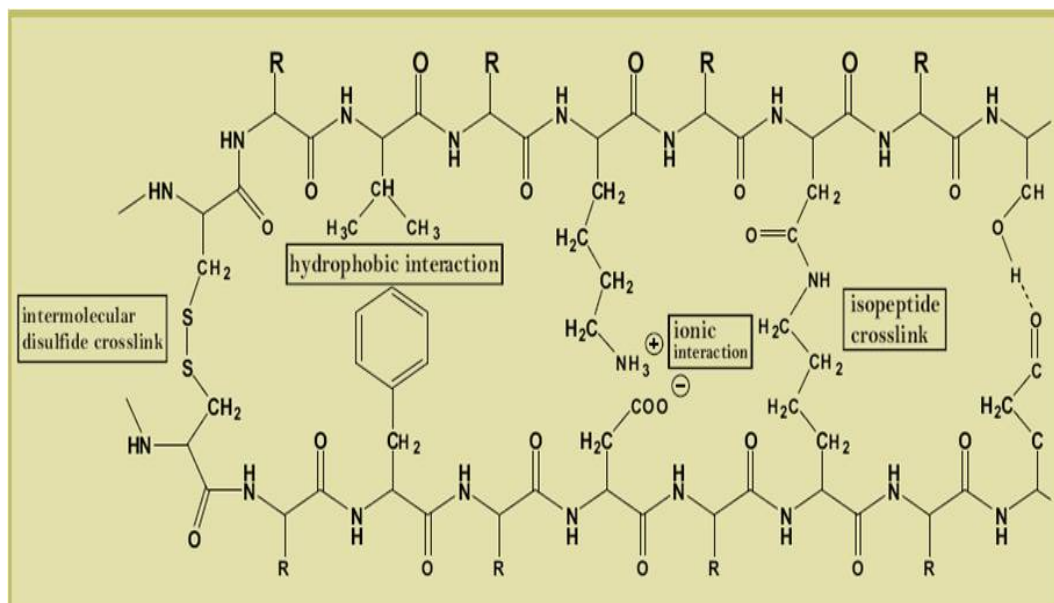


Figure 4.5: Schematic representation of bonds in wool.

From Figure 4.6, it can be seen that there is hysteresis in moisture absorption, with the desorption curve being higher than the absorption curve. The shorter intermediate curves show the changeover from absorption to desorption at different humidities. Regain at given relative humidities varies

with temperature, for example, at 70% RH, values between 17 and 18% were found from -29 °C to 4 °C, but then fell to 13% at 17 °C [41].

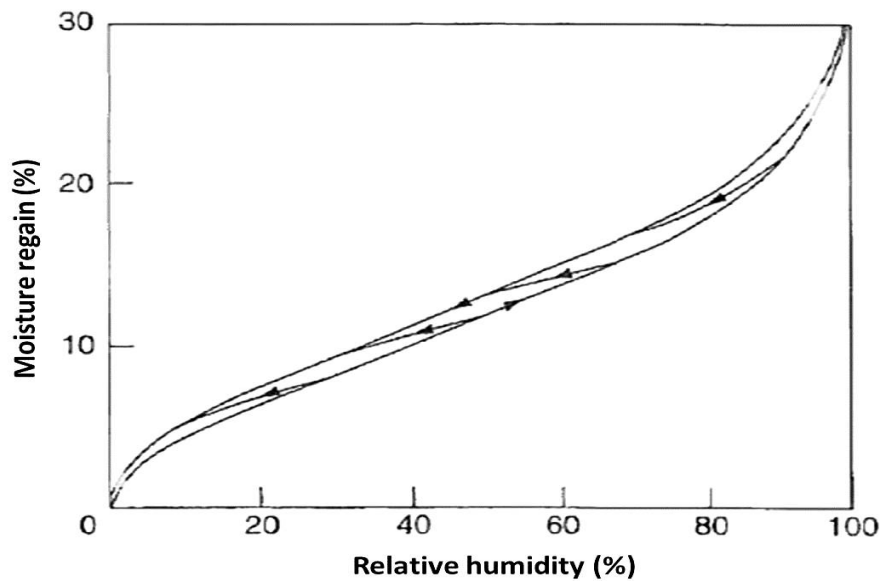


Figure 4.6: Change of moisture regain of wool with humidity – after [42].

When wool takes up water, the swelling is almost entirely radial, with little change in length. Table 4.5 shows a set of values for radial and volume swelling, together with the change in fibre density [43].

The swelling behaviour is explained on the presumption that most or all of the water is absorbed by the matrix, due to the presence of accessible hydrophilic groups, and that this increases the lateral spacing between fibrils, whose lengths do not change. The first molecules to be absorbed can pack efficiently with the protein molecules, but later ones merely increase the volume.

Table 4.5: Moisture absorption and swelling of wool. After [43]

Moisture re- gain (%)	0	2	5	7	10	15	20	25	30	33
Radial swelling (%)	0	0.66	1.82	2.62	4.00	6.32	8.88	11.7	14.6	16.3
Volume swelling (%)	0	1.57	4.24	6.10	9.07	14.3	20.0	26.2	32.8	36.8
Density (g/cm ³)	1.304	1.310	1.314	1.315	1.315	1.313	1.304	1.291	1.277	1.268

The quality of chemically treated fibres strongly depends on their wetting properties. These fibres are modified by the location of chemically active elements contributing to their structural properties of natural and artificial origin at different water contents. Various chemical treatment processes are applied to the wool pre- and post-woven [37]. Analysis of the quality of the product, in terms of strength, texture, flexibility, improved hydrophilic/hydrophobic and/or oleophobic properties, are undertaken through internationally accorded testing procedures. The process is empirical, in that, there is a lack of understanding of the underlying material modification at the atomic/molecular level leading to the investigations using small-angle scattering techniques.

Chapter 5

Experiments

5.1 Introduction

Different wool fibre samples were provided by BKB in Port Elizabeth. Those from goats (mohair) have the prefix M in the data presented here. The difference in the samples are their diameters which are known to be in the ranges from 25 to 38 μm .

Through a combination of SANS and SAXS, study of physical and chemical properties of textile fibres during dry and heavy water wet was carried out. Samples were obtained in South Africa for analysis by SANS overseas as well as SAXS. Details of the experimental set-up are discussed below.

5.2 SANS

5.2.1 Introduction

SANS experiments were only carried out at Yellow Submarine SANS as the Necsas SANS was not fully operational. Characteristics of Yellow Submarine SANS are already presented in Table 3.2.

5.2.2 Aim

To study the nano structure of mohair fibres by comparing different types of fibres using SANS technique. The structure was enhanced by contrast variation using D_2O .

5.2.3 Procedure

2 cm (with different diameter of $37.8 \mu m$ (M4), $25.5 \mu m$ (M5) and $25.3 \mu m$ (M1097)) long dry and wet fibres were used. The samples M4 and M5 were also washed of fat by carbon tetrachloride (CCl_4). They were weighed, packed into thin walled quartz tube container with the fibres predominantly aligned by stretching on both ends of the tube as shown in Figure 5.1. They were then exposed to a beam of cold neutrons with a defined wavelength of 3.88 \AA (defined by NVS speed of 6000 rpm). Measurements were done for dry, 10 and 20% wet (D_2O -deuterated) for each sample. The 10% deuteration did not show any change in scattering picture compared to dry samples. This was probably due to low D_2O content. Samples were measured at the shortest (0.98 m) and longest (5.5 m) sample detector distance (S-D) access-

ible from the instrument. Results of the spectra are shown in the following section.



Figure 5.1: SANS sample set-up of the fibres in a quartz tube stretched on both ends for alignment.

5.2.4 Results

Figure 5.2 shows 2-D SANS spectra recorded for $25.5 \mu\text{m}$ (M5) samples that are clean and dry (a.), dirty and dry (b.), clean and wet (c.) as well as dirty and wet (d.), respectively (using the GRASP software [28]).

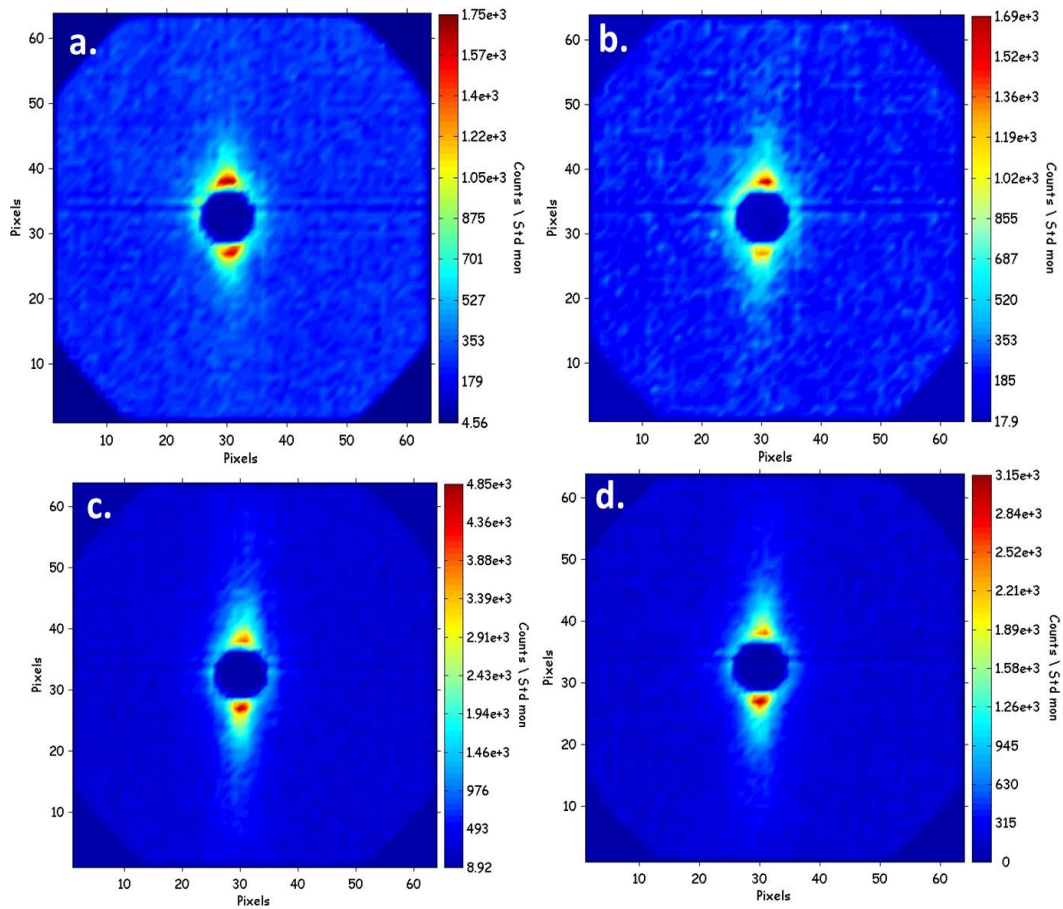


Figure 5.2: SANS spectra obtained for 25.5 μm diameter mohair fibres (M5), collected from BNC facility: (a.) Clean and dry, (b.) Dirty and dry, (c.) Clean and wet, and (d.) Dirty and wet.

Figure 5.3 also shows 2-D spectra for three different samples under D_2O wet conditions.

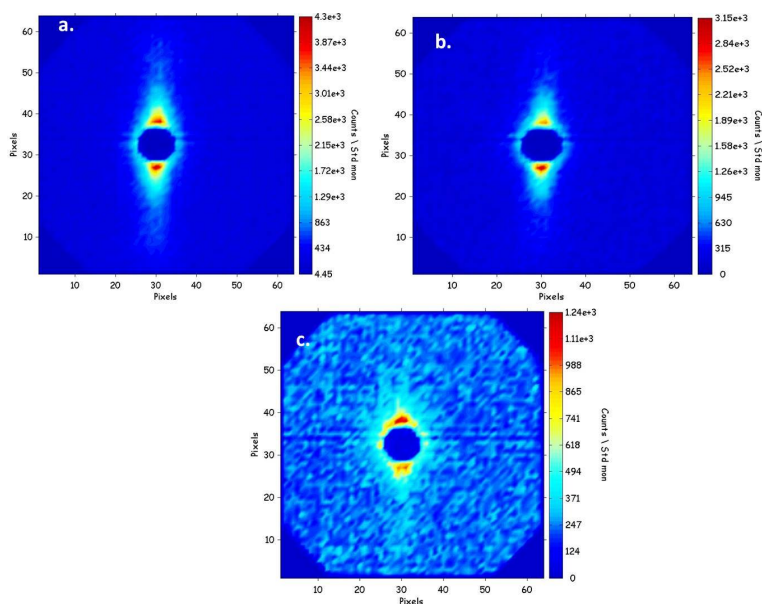


Figure 5.3: Spectra showing (a.) M4, (b.) M5 and (c.) M1097 samples, respectively, both wet with 20% D₂O.

5.2.5 Discussion

The anisotropy in Figure 5.2a. and Figure 5.2b. is different, showing that CCl₄ treatment enhanced the structure, i.e. it can be inferred that both samples might have had different fat content. This is due to scattering visible in Figure 5.2b., which is not visible in Figure 5.2a.

Figure 5.3a. and Figure 5.3b. exhibit similar anisotropy, hence the discussion in Chapter 6 will only be concentrated on discussing samples of Figure 5.3b. and/or Figure 5.3c. for samples M5 and M1097, respectively due to their comparable diameters. Detailed discussions are presented in Chapter 6.

5.3 SAXS

SAXS experiments were carried out at the Australian Synchrotron SAXS. A point collimation was used since it can be used to analyse anisotropic samples, such as fibres or porous solids. Unlike a line collimation (suitable for isotropic samples), a point collimation allows one to probe small sample areas and determine their local nano-structure, with the drawback of longer measuring times at low flux facilities.

5.3.1 Aim

To study the nano structures of different mohair fibres for comparison with SANS data.

5.3.2 Procedure

Fibre sample (M5) was mounted on a sample holder and inserted in a SAXS beam line and illuminated for 10 seconds due to high intensity of the beam.

5.3.3 Results

Figure 5.4 shows a spectrum obtained. Reduction and analysis of the data are discussed in Chapter 6.

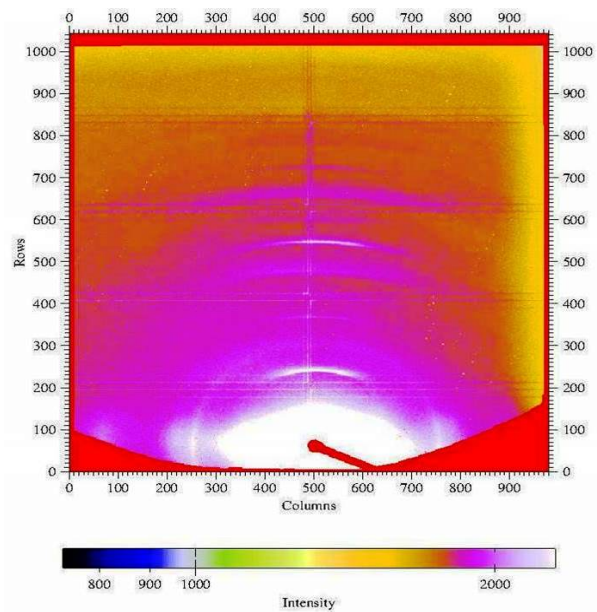


Figure 5.4: SAXS spectra obtained from mohair fibres, collected at the Australian Synchrotron SAXS instrument.

Chapter 6

Results and Discussions

6.1 Introduction

This chapter presents the overall results and discussions of the work carried out during the study of wool fibres using both SANS and SAXS. It also presents possible applications that can be studied using SANS facilities.

6.2 Study of Wool Fibres

6.2.1 SANS

For SANS spectra, there is an anisotropic feature observed in different wool fibre samples. This feature is not observed in the SAXS spectrum as shown in Figure 5.4. This is one of the reasons to use both techniques to study the structure (refer to Chapter 2).

As already highlighted in Section 5.2.4, Figure 5.3(*a*) and (*b*) show similarity with their anisotropy, thus the discussion will only focus on the M5

and M1097 samples which are also comparable in fibre diameter.

The spectra were sectored, both horizontally and vertically as shown in Figure 6.1. The horizontal sectors correspond to the in-line orientation of the fibres, while the vertical sectors are perpendicular to the direction of the fibres as placed in the beam.

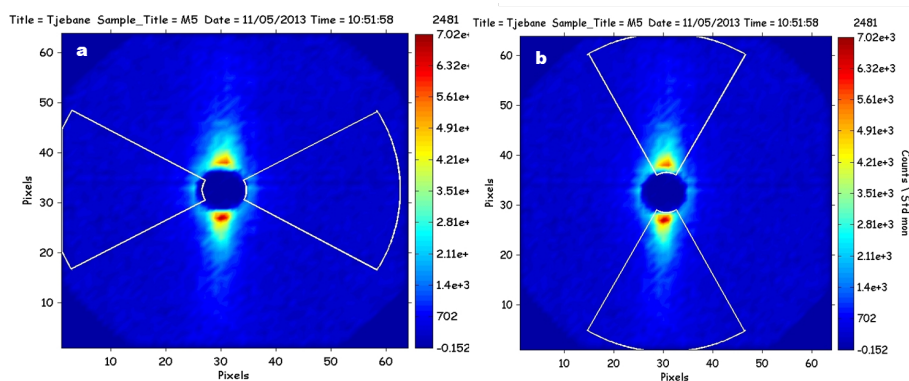


Figure 6.1: Spectra from M5 wet samples (a) dirty and (b) clean. The spectra are sectored, (a) -along the fibre and (b) -perpendicular to the fibre, for further analysis.

The data is then plotted for intensity, $I(q)$ versus q for the whole q -range studied, i.e. merging the short and long sample-detector distances (Figure 6.2) for comparison and extraction of gyration radii, as discussed below.

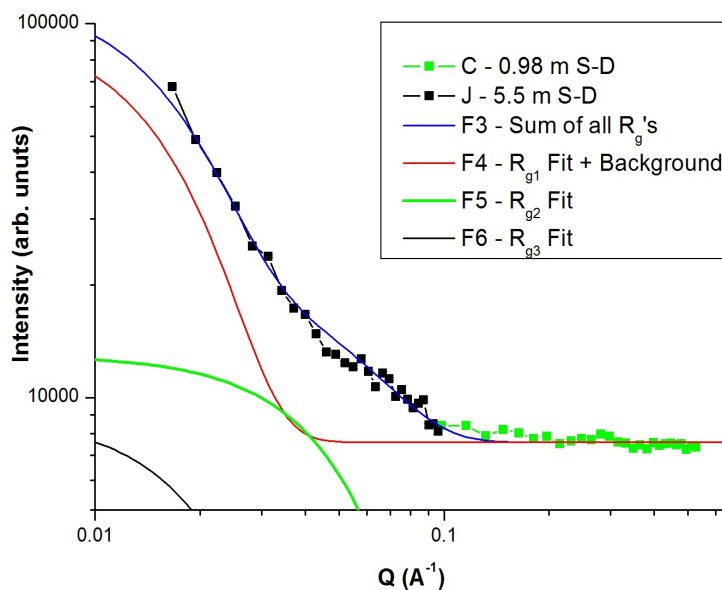


Figure 6.2: A plot of $I(q)$ versus Q for a 20% D_2O -wet wool showing short (C) and long (J) accessible sample to detector distance merged, the 3-fitting components (F4, F5 and F6) as well as their sum (F3) using equation 6.1.

Figure 6.3 shows a plot of intensity, $I(q)$ versus q for same sample (M5) that is wet and dry and both fitted according to the Guinier approximation,

$$I(q) = \sum_{n=1}^3 \left(I_n(0) \times e^{-(qR_{gn})^2/3} \right) + I_{bg} \quad (6.1)$$

where $I(q)$ is the total intensity, $I_n(0)$ for $n = 1, 2, \dots$ is the intensity at $q = 0$ for both positions, R_{gn} are gyration radii (computed about the particle centroid) observed at the total instrument length range and I_{bg} is the background intensity (Table 6.1).

The Guinier approximation method is a quantitative analysis of particle size and shape applicable to the low q -limit measurements (i.e. $0 < q < 1/R_g$), which is the case for the measurements made above.

Also Figure 6.1 shows a plot of intensity, $I(q)$ versus q for samples (M5) that are both wet. The difference in these samples was (a) is dirty while (b) was cleaned using CCl_4 as highlighted above. The data was also fitted and the results were presented in Table 6.2.

This procedure was also repeated for the rest of the samples with different conditions, however discussion in Section 6.3 is only concentrated on sample M5.

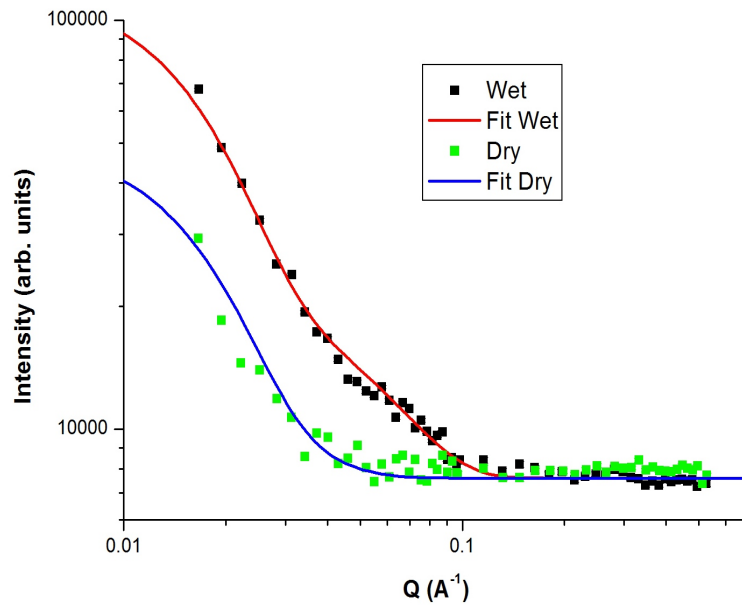


Figure 6.3: Scattered intensity as a function of Q for data sectors perpendicular to the fibres at different conditions from M5 sample.

Table 6.1: Data plot and fitting of M5 wet and dry samples along the perpendicular (vertical sectors) direction of the fibres as extracted from Figure 6.3.

Sample	I_{bg}	Intensity I_1 / Radius R_{g1} (Å)	Intensity I_2 / Radius R_{g2} (Å)	Intensity I_3 / Radius R_{g3} (Å)
Wet vertical	$7600. \pm 87.2$	$91000. \pm 301.7 /$ 101.0 ± 10.0	$13000. \pm 114. /$ 70.0 ± 8.4	$8950. \pm 95. /$ 29.8 ± 5.5
Dry vertical	$7600. \pm 87.2$	$39900.0 \pm 199.7 /$ 97.0 ± 9.8	$8900.0 \pm 94.3 /$ 59.8 ± 7.6	$4050.0 \pm 89. /$ 53.0 ± 7.3

6.2.2 SAXS

Figure 6.5(a) shows a spectrum, obtained from Australian synchrotron (AS) SAXS with radial sector (shown in black) that produced a plot of I versus q

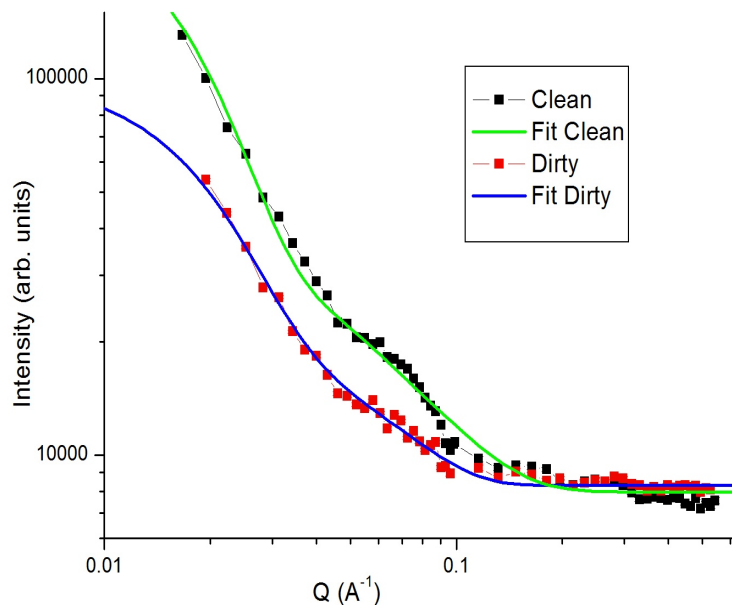


Figure 6.4: Scattered intensity as a function of Q for data sectors perpendicular to the fibres that are clean and dirty, both wet with 20% D_2O from sample M1097.

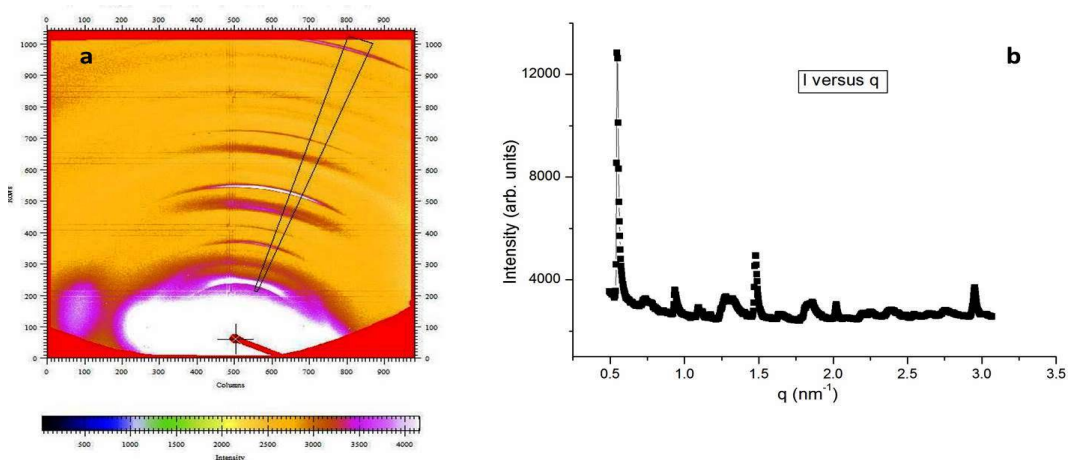
shown in Figure 6.5.b. The peaks are associated with different structures of the fibre, although there is no proper model to fit to the data.

6.3 Discussion

Table 6.1 shows different gyration radii observed for M5 clean sample wet with D_2O and dry as plotted and fitted in Figure 6.3, using the Guinier approximation model (eq. 6.1). Although the model does not perfectly fit the data due to the fact that the samples were not fully diluted as the model requires, it shows in approximation, the radii of gyration that can be observed using SANS technique. However, out of three structures observed, two larger ones show an increase in size by approximately 10% from dry to

Table 6.2: Data plot and fitting of M1097 wet sample along the perpendicular (vertical sectors) direction of the fibres as extracted from Figure 6.4.

Sample	I_{bg}	Intensity I_1 / Radius R_{g1} (\AA)	Intensity I_2 / Radius R_{g2} (\AA)	Intensity I_3 / Radius R_{g3} (\AA)
Dirty vertical	$8300.\pm 91.1$	$70282.\pm 265.1$ / 90.2 ± 9.5	12984 ± 114 / $40.\pm 6.3$	9946 ± 99 / 26.1 ± 5.1
Clean vertical	$6400.\pm 80.$	$200000.\pm 447.$ / $100.\pm 10$	$9000.\pm 300.$ / $60.\pm 7.7$	$8000.\pm 89.4$ / 24.1 ± 4.9


 Figure 6.5: Spectrum (a.) and a plot of a radial average for I versus q (b.) for fibre sample obtained from a AS .

wet. The structures (radii of gyration in Table 6.1) are respectively related to microfibril, matrix and microfibril, as shown in Figure 4.3.

Table 6.2 shows different radii of gyration observed for D_2O wetted M1097 clean and dirty samples as extracted in the fit in Figure 6.4. The radii of gyration observed for R_{g1} and R_{g2} are different, with the clean sample exhibiting larger structures for both. This is attributed to the dirt that suppresses the features in the sample. However R_{g3} does not differ significantly. It

can be concluded that cleaning the samples with CCl_4 solution improves the contrast of the samples.

Franklyn *et al.* [44] studied similar samples and observed that for dry samples's main sizes are in both directions, i.e. vertical and horizontal, while in the wet samples at room the smallest characteristic distance is reduced roughly to $1/3$ while the second one is reduced by the factor of 1.5, and the third one is reduced by factor of 1.2. That is an indication that a substantial rearrangement of internal structure of wool fibres occurs during wetting. On the other hand during the wetting, they observed new patterns showing an inner distance 5.2 \AA and 30.1 \AA . These patterns were not seen in dry samples. Similar inner distances were observed by SAXS [36] where d spacing 80 , 46 and 28 \AA were reported. These differences are explained by the different samples and different dry/wet states. These values correspond to the microfibril size.

Interpretation of the data in terms of determining radius of gyration as a function of the supermolecular shape requires additional data as a function of fibre diameter as well as conditions under which the fibres have been treated.

There is currently no model available to fit the SAXS data due to the fact that the wool fibres were analysed in a bundle instead of a single strand and a smaller collimation of the beam in the range of $1\text{--}5 \mu\text{m}$ is required, however this can only be achieved in the case of a synchrotron SAXS due to high intensities as shown by Kajiura, *et al.* [36] and evidenced in Figure 6.5(a)

6.4 SANS Applications

The SANS technique can be applied to different fields of science. For complex macromolecular structures like viruses, SANS can be combined with the contrast variation technique to gain structural information about the protein, nucleic acid and lipid components separately. This makes it possible for biological samples to be analysed under physiological conditions and the data obtained can reveal in-situ structural information. Few examples of SANS applications in different fields are listed below:

Biological Applications

- Determination of shape and subunit organisation of the DNA Methyltransferase (M.AhdI) [45].

The M.AhdI enzyme has been prepared with deuterated S subunits, to allow contrast variation for study using SANS method. The radius of gyration (R_g) and maximum dimensions (D_{max}) of the M subunits in situ in the multisubunit enzyme (50 Å and 190 Å, respectively) were found to be close to those of the entire MTase (51 Å and 190 Å). In contrast, the S subunits in situ have experimentally determined values of $R_g = 35$ Å and $D_{max} = 110$ Å, indicating their more central location in the enzyme.

- The MS2 coat protein shell is likely assembled under tension: A novel role for the MS2 bacteriophage, a protein as revealed by SANS [46].

Recombinant forms of the bacteriophage MS2 and its RNA-free

(empty) MS2 capsid were analysed in solution to determine if RNA content and/or the A (or maturation) protein play a role in the global arrangement of the virus protein shell. Using SANS method, analysis of the (coat) protein shell of recombinant versions of MS2 that lack the A protein revealed dramatic differences compared to wild-type MS2 in solution.

Polymer Science Applications

- Using a small-angle neutron scattering technique, sodium dodecyl sulfate-poly (propylene oxide) methacrylate mixed micelles were studied [47].

Mixed micelle of protonated or deuterated sodium dodecyl sulfate (SDS and SDSd25, respectively) and poly(propylene oxide) methacrylate (PPOMA) were studied by SANS method. In all the cases the scattering curves exhibit a peak whose position changes with the composition of the system. The analysis confirms the particular core-shell structure of the SDS-PPOMA mixed micelle, i.e., a SDS "core" micelle surrounded by the shell formed by PPOMA macromonomers. The structural parameters of mixed micelles obtained from the analysis of the SANS data were in good agreement with those determined previously by conductimetry and fluorescence studies.

Material Science and Engineering Applications

- Analysis of the precipitation behaviour in a high-speed steel by means of SANS technique [48]

SANS is a suitable technique for characterisation of precipitation reactions especially at the early stages when precipitates are too small for transmission electron microscopy (TEM). Here, SANS was used to study the precipitation reactions in the steel grade HS6-5-2 during isothermal tempering at 590 °C and it was found that three different populations of precipitates with different sizes were present. A large number of small precipitates with radii around 0.7 nm were already formed after 10 minutes of tempering in the first size range (particles less than 1 nm).

Chapter 7

Conclusions

7.1 Summary of the work

A SANS facility has been developed and demonstrated at Necsa using silver behenate (AgBeh) and the results were compared with that of BNC (Yellow Submarine). The facility is currently being expanded by installing curved neutron guides as well as a long scattering chamber.

Measurements of polymers (wool fibres in this work) were also performed at the Yellow Submarine SANS. The results as shown in Chapter 6 reveal interesting features which were not seen with other techniques, such as SAXS.

- It has been demonstrated that a SANS capabilities can be developed and implemented at Necsa as shown, using AgBeh as a standard sample in comparison with BNC SANS setup.
- The modelling of the facility has been demonstrated, and the facility is being implemented. The model made a good benchmark towards the

development of the low signal-to-noise ratio facility at Necsca.

- SANS measurements were carried out on different types of wool at BNC SANS facility, and could achieve a good agreement with structure measured with complementary SAXS technique [36].
- The wetting process on different wool fibres was also investigated. It was found that the D_2O penetrates into a deep structure of wool building up a fibre-water regular structure. A proper model needs to be developed to fit the data for exact structure determination, however with a similar model fitting, structures related to fibre components are observed.
- As given in the examples of SANS applications (Section 6.4), it is clear that there is a need for a SANS facility to be established for the science community in South Africa.

7.2 Recommendations

Most of the work in terms of modelling and designing of a complete SANS facility has been completed. The future is to construct the scattering hall, extending the scattering chamber, installation of the curved neutron guide as well as installation of a minimum shielding outside of the reactor hall due to the curved guide. A bigger sample holder will also be installed to accommodate different types of sample and their weights.

It will also be of interest to look at the flux on the target whether the magnetic characteristics cannot be investigated using this facility, but this

will require some more work in terms of installing polarisers on the beam line.

For wool fibre samples

- Proper sample holders have to be developed for aligning the wool fibres with same amount of tension and making the fibres to be flat-aligned,
- Data fitting model has to be developed for this special samples,
- Moisture regain of the fibre has to be studied, and
- Different cleaning agents have to be applied to the wool fibres to study different mechanical properties of the fibres.

Bibliography

- [1] D. Aisa, S. Aisa, E. Babucci, F. Barocchi, A. Cunsolo, A. De Francesco, F. Formisano, T. Gahl, E. Guarini, A. Laloni, H. Mutka, A. Orecchini, C. Petrillo, W. Pilgrim, A. Piluso, F. Sacchetti, J. Suck & G. Venturi. BRISP: A new thermal-neutron spectrometer for small-angle studies of disordered matter. *Journal of Non-Crystalline Solids*, 352:5130 – 5135, 2006.
- [2] A. Ashray. Optimization study for small angle neutron scattering spectrometer the ET-RR-1 reactor. *Nuclear Instruments and Methods in Physics Research B*, 219:519–526, 1997.
- [3] R. Gilles, A. Ostermann & W. Petry. Monte carlo simulations of the new small-angle neutron scattering instrument SANS-1 at the Heinz Maier-Leibnitz Forschungsneutronenquelle. *Journal of Applied Crystallography*, 40:s428–s432, 2007.
- [4] E. P. Gilbert, J. C. Schulz & T. J. Noakes. Quokka: The Small-Angle Neutron Scattering Instrument at OPAL. *Physica B*, 385–386:1180–1182, 2006.
- [5] S. W. Lovesey. *Theory of Neutron Scattering from Condensed Matter*. Oxford Science Publications, 1996.
- [6] B.T.M. Willis & C.J. Carlile. *Experimental Neutron Scattering*. Oxford University Press Inc., 2009.
- [7] M. Bischof, P. Staron, A. Michels, P. Granitzer, K. Rumpf, H. Leitner, C. Scheu & H. Clemens. The influence of spin-misalignment scattering on the SANS data evaluation of martensitic age-hardening steels. *Acta Materialia*, 55:2637 – 2646, February 2007.
- [8] R. Borsali & R. Pecora. *Soft-Matter Characterization*, volume 1. Springer, 2008.

- [9] R. Pynn. Neutron scattering. In *A Primer*, volume 19. LAUR-95-3840 Los Alamos Science, 1990.
- [10] P. Reuss. *Neutron Physics*, chapter 3. EPD Sciences, 2008.
- [11] G. L. Squires. *Introduction to the Theory of Neutron Scattering*. USA Dover, 1997.
- [12] J. Wakefield, R. M. Jones & A. T. Leath. DoE nixes neutron source; Leaves other cuts to Congress. *Eos Trans. AGU*, 76(8):77–78, 1995.
- [13] J. Fitter, T. Gutberlet & J Katsaras. *Neutron Scattering in Biology*. Springer, 2006.
- [14] V.L. Aksenov. Update on the pulsed reactor IBR-2 and its instruments at Dubna. *Physica B: Condensed Matter*, 174(14):438 – 442, 1991.
- [15] B. Hammouda. A Tutorial on Small-Angle Neutron Scattering From Polymers, June 1995.
- [16] B. Hammouda. Probing Nanoscale Structures: The SANS Toolbox, 2000.
- [17] A. J. Jackson. Introduction to Small-Angle Neutron Scattering and Neutron Reflectometry, May 2008.
- [18] N. Zettili. *Quantum Mechanics Concepts and Applications*. A John Wiley and Sons, Ltd., Publication, second edition, 2009.
- [19] K. Mortensen. *Structural Studies of Polymer Systems Using Small-Angle Neutron Scattering*, volume 2. Gordon and Breach Science Publishers, Condensed Matter Physics and Chemistry Department, Risø National Laboratory, DK-4000 Roskilde, Denmark, 2001.
- [20] D. K. Arrowsmith & C. M. Place. *Ordinary Differential Equations*. Chapman and Hall, 1982.
- [21] T. N. Blanton, C. L. Barnes & M. Lelental. Preparation of silver behenate coatings to provide low- to mid-angle diffraction calibration. *Journal of Applied Crystallography*, 33(1):172–173, 2000.
- [22] R. Gilles, U. Keiderling & A. Wiedenmann. Silver behenate powder as a possible low-angle calibration standard for small-angle neutron scattering. *Journal of Applied Crystallography*, 31(6):957–959, 1998.

- [23] T. C. Huang, H. Toraya, T. N. Blanton & Y. Wu. X-ray powder diffraction analysis of silver behenate, a possible low-angle diffraction standard. *Journal of Applied Crystallography*, 26(2):180–184, Apr 1993.
- [24] A.C. Finnefrock. SAXS Calibrants (http://bigbro.biophys.cornell.edu/documents/sax_calibrants/saxs_sphere.html accessed on 01 August 2014), January 2000.
- [25] B. P. McAlister, B. C. & Grady. Simulation of small-angle x-ray scattering from single-particle systems. *Journal of Applied Crystallography*, 31(4):594–599, 1998.
- [26] A.V. Poutchkov. Optimization of Velocity Monochromators for Low Power Research Reactors. Report, Institute for Physics and Power Engineering, Bondarenko sq. 1, Obninsk 249020, Kaluga Region, Russian Federation, March 2003.
- [27] S. R. Kline. Reduction and analysis of SANS and USANS data using IGOR Pro. *Journal of Applied Crystallography*, 39(6):895–900, 2006.
- [28] C. Dewhurst. *Graphical Reduction and Analysis SANS Program for MatlabTM*. Institute Laue Langevin, Grenoble, France, 2003.
- [29] S. Forster, L. Apostol & W. Bras. Scatter: Software for the Analysis of Nano- and Mesoscale Small-Angle Scattering. *Journal of Applied Crystallography*, 43(3):639–646, 2010.
- [30] J. Kohlbrecher & I. Bressler. *Software package SASfit for fitting small-angle scattering curves*. Laboratory for Neutron Scattering - Paul Scherrer Institut, CH-5232 Villigen PSI, Switzerland, January 2011.
- [31] L. Almásy, A. Len, M. Markó & E. Rétfalvi. Wavelength calibration in conventional SANS setup with a mechanical velocity selector. *Z. Kristallogr. Suppl.*, 23:211–216, 2006.
- [32] Gy. Török. Modelling of SAFARI SANS Facility. IAEA Expert Mission, April 2009.
- [33] G. Zsigmond, K. Lieutenant & F. Mezei. Monte Carlo simulations of neutron scattering instruments by VITESS: Virtual instrumentation tool for ESS. *Neutron News*, 13(4):11–14, 2002.
- [34] H. Höcker. *Wool: Science and Technology*. Woodhead Publishing Limited, 2002.

- [35] H. J. Woods. The Structure of Textile Fibres. III.-Fibre Properties and Molecular Arrangement. *Journal of the Textile Institute Proceedings*, 40(4):P363–P369, 1949.
- [36] Y. Kajiura, S. Watanabe, T. Itou, A. Iida, Y. Shinohara & Y. Amemiya. Structural Analysis of Single Wool Fibre by Scanning Microbeam SAXS. *Journal of Applied Crystallography*, 38(3):420–425, June 2005.
- [37] L. Kreplak, A. Franbourg, F. Briki, F. Leroy, and D. Dallè & J. Doucet. A new deformation model of hard α -keratin fibers at the nanometer scale: Implications for hard α -keratin intermediate filament mechanical properties. *Biophysical Journal*, 82(4):2265 – 2274, 2002.
- [38] R. C. Marshall & J.M. Gillepsie. The Keratin Proteins of Wool, Horn and Hoof from Sheep. *Australian Journal of Biological Sciences*, 30(5):389–400, 1977.
- [39] M. V. Preston, J. M. & Nimkar. Measuring The Swelling of Fibres in Water. *Journal of the Textile Institute Proceedings*, 40(7):674–688, 1949.
- [40] N. S. Wooding & S. H. Atlas. *Chemical After-treatment of Textiles*. Wiley-Interscience, a Division of John Wiley and Sons, Inc., 1971.
- [41] R. C. Darling & H. S. Belding. Moisture Adsorption of Textile Yarns at Low Temperatures. *Industrial and Engineering Chemistry*, 38(5):524–529, 1946.
- [42] J. B. Speakman & E. Stott. Part II-The Influence of Drying Conditions on the Affinity of Wool for Water. *Journal of the Textile Institute Transactions*, 27(7):T186–T190, 1936.
- [43] WIRA. Wool Research Vol 2: Physical Properties of Wool Fibres and Fabrics. Wool Industry Research Association, Leeds, 1955.
- [44] C. B. Franklyn & Gy. Török. Use of small angle neutron scattering to study various properties of wool and mohair fibres. *AIP Conference Proceedings*, 1412(1):93–97, 2011.
- [45] P. Callow, A. Sukhodub, J. E. Taylor & G. G. Kneale. Shape and Subunit Organisation of the DNA Methyltransferase M.AhdI by Small-angle Neutron Scattering. *Journal of Molecular Biology*, 369:177–185, March 2007.

- [46] D. A. Kuzmanovic, I. Elashvili, C. Wick, C. O'Connell & S. Krueger. The MS2 Coat Protein Shell is Likely Assembled Under Tension: A Novel Role for the MS2 Bacteriophage A Protein as Revealed by Small-angle Neutron Scattering. *Journal of Molecular Biology*, 355:1095–1111, 2006.
- [47] G. Bastiat, B. Grassl, O. Borisov, A. Lapp & J. Francois. A small-angle neutron scattering study of sodium dodecyl sulfate-poly(propylene oxide) methacrylate mixed micelles. *Journal of Colloid and Interface Science*, 295(2):417 – 426, 2006.
- [48] H. Leitner, P. Staron, H. Clemens, S. Marsoner & P. Warbichler. Analysis of the precipitation behaviour in a high-speed steel by means of small-angle neutron scattering. *Materials Science and Engineering A*, 398:323–331, March 2005.